nature chemical biology

Article

https://doi.org/10.1038/s41589-026-02165-6

Mast cell extracellular granules are bioactive condensates assembled by heparin and polyamine

Received: 30 April 2025

Accepted: 5 February 2026

Published online: 27 February 2026

Check for updates

Yiwei Xiong[1], Dylan T. Tomares[2], Jianjian Guo[1], Kazuki Sato[1], Longhui Zeng[1], Yuan Tian[1], Maohan Su[1], Ava Albis[1], Avnika Pant[2], Rohit V. Pappu[2] ✉ & Xiaolei Su[1,3,4,5,6,7] ✉

Biomolecular condensates are membraneless bodies that organize biochemical reactions typically within cells. However, the roles of condensates in extracellular space—where conditions differ substantially from intracellular space—remain poorly understood. Here we report that mast cell extracellular granules (MCEGs), a stable membraneless entity, are condensates assembled through electrostatic interactions between glycosaminoglycans and polyamines. Disrupting polyamine synthesis or trafficking blocks MCEG formation and compromises the storage of proteases and cytokines. Granules reconstituted with heparin and spermine are sufficient to enrich mediators such as carboxypeptidase A3 (CPA3) and tumor necrosis factor (TNF), maintaining an elevated pH and higher concentrations of calcium and zinc compared to the extracellular milieu. This unique environment enhances CPA3 enzymatic activity. Furthermore, the granules increase TNF binding and its bioactivity toward endothelial cells. Together, we reveal MCEGs as functionally active biomolecular condensates with distinct biochemical and immunological properties; MCEGs are formed through sugar–metabolite interactions, expanding the mechanisms of condensate assembly beyond classical protein–protein and protein–RNA interactions.

Biomolecular condensation governs the spatial and temporal organization of the intracellular space by forming membraneless structures such as nucleoli[1–4], nuclear speckles[5], stress granules[6–8] and immune signaling clusters[9–14]. Condensation can be mechanistically realized through a combination of reversible site-specific binding, percolation involving hierarchies of multivalent homotypic and heterotypic interactions and solubility considerations that drive phase separation[1,10,15–18]. However, two major aspects of condensation have not received much attention. First, with a few exceptions[19–22], the possibility of condensation having a role in spatial and temporal organization of macromolecules and biochemical reactions in extracellular spaces has not been considered. Second, in cells and tissues, complex coacervation, as opposed to phase separation driven mainly by homotypic interactions among intrinsically disordered proteins, is likely to be the most important contributor to phase separation in multicomponent systems comprising highly charged molecules that form compositionally distinct or multiphase biomolecular condensates[8,23–38]. Complex coacervation is driven by system-specific and solution-condition-dependent hierarchies of heterotypic interactions[25–27,31–33,39,40]. The extracellular space has a distinct chemical environment in terms of its pH and compositions

[1]Department of Cell Biology, Yale School of Medicine, New Haven, CT, USA. [2]Department of Biomedical Engineering, Center for Biomolecular Condensates, James McKelvey School of Engineering, Washington University in St. Louis, St. Louis, MO, USA. [3]Yale Cancer Center, New Haven, CT, USA. [4]Yale Center for Immuno-Oncology, New Haven, CT, USA. [5]Yale Center for Systems and Engineering Immunology, New Haven, CT, USA. [6]Yale Stem Cell Center, New Haven, CT, USA. [7]Yale Liver Center, New Haven, CT, USA. ✉e-mail: pappu@wustl.edu; xiaolei.su@yale.edu

of ions and metabolites, which indicates a separate set of mechanisms for complex coacervation. Here, we present results from studies of extracellular granules of mast cells[41] as archetypal systems to explore how condensation influences spatial organization and functions of biomolecules in the extracellular space.

Mast cells are long-lived immune cells that reside in tissues close to host–environment interfaces, such as the skin, intestinal and pulmonary mucosa[42]. They are well known for their innate capabilities as responders to allergic inflammation and pathogen infections[43,44]. There is also growing interest in the roles of mast cells in host-protective behavior through crosstalk with neurons[45–47]. Central to these versatile functions are mast cell granules, which are membrane-bound intracellular vesicles that serve as storage reservoirs of preformed bioactive mediators, including cytokines, chemokines, proteases, lipids, biogenic amines and proteoglycans[48]. Upon activation by allergens, pathogens or environmental stimuli, intracellular granules undergo exocytosis, during which the membrane coat is shed and stored mediators are released into the extracellular space[49,50]. While some mediators, such as histamine, are released in a soluble form, other mediators, including tumor necrosis factor (TNF)[41], interleukin 1β (IL-1β)/pro-IL-1β (ref. 51), tryptase[52], chymase and heparin proteoglycans[53,54], remain embedded in the membraneless 'granule remnants' (ref. 55). These granule remnants, called mast cell extracellular granules (MCEGs), are stable micron-sized bodies and readily observed under the microscope[56,57]. These MCEGs not only modulate macrophage and dendritic cell functions locally[58,59] but also enter the blood and lymphatic vessels to induce immune response remotely[41,60]. However, the molecular mechanism for maintaining these membraneless MCEGs in the extracellular space remains unclear. The lack of this knowledge also impedes understanding of the benefits of maintaining mediators in the granule versus in the soluble format.

Heparin and chondroitin sulfate glycosaminoglycans are the major components of mast cell granules[48,61]. Heparin is synthesized selectively in mast cells[48]. Genetic deletion of key heparin-synthesizing enzymes such as Ndst2 or glycosyltransferase Exostosin 1 impairs granule formation[62–64], highlighting the essential role of heparin in granule assembly. Furthermore, because of the highly negative charge of heparin[65], positively charged cargo proteins may, thus, complex with heparin through electrostatic interactions. Recent studies showed that cell surface heparan sulfate promotes the condensation of highly basic proteins such as basic fibroblast growth factor (bFGF)[66] and C–C motif chemokine ligand 5 (CCL5)[22]. However, these proteins are not the major components of MCEGs. Nevertheless, the studies on condensates formed by heparan sulfate and bFGF/CCL5 inspired us to test the possibility that the negatively charged heparin can undergo coacervation with positively charged biomolecules in MCEGs to drive condensate formation, thus providing the structural basis for the assembly of membraneless MCEGs.

Here, we report that MCEGs are formed through the condensation between heparin and polyamine. Using reconstitution approaches, we showed that condensates containing heparin and spermine create a distinct electrochemical microenvironment characterized by elevated pH and enriched metal ions. Notably, this specialized environment enhances the enzymatic activity of protease carboxypeptidase A3 (CPA3), a major component of MCEGs. TNF in the granular form also shows a higher activity in stimulating endothelial cells as compared to the soluble format. Collectively, these findings reveal MCEGs as functionally active condensates that serve as storage depots while enabling the catalysis of biochemical reactions and mediating immune response.

Results

Polyamines form condensates with heparin

Heparin, a glycosaminoglycan, is synthesized by mast cells and stored in mast cell granules[48], where its concentrations range from a few to a hundred micromolar[67,68]. Heparin is a flexible polyanion that, by some estimates, has an excess charge of −3.3 per disaccharide unit[65]. This derives from the numerous sulfate groups that modify the long backbone[69]. Consequently, the heparin interaction with polyvalent counterions is expected to drive the formation of membraneless condensates through complex coacervation[24]. To test this hypothesis, we mixed heparin with monovalent, divalent or polyvalent cations at physiologically relevant concentrations. Upon mixing, heparin formed spherical condensates with spermidine and spermine (Fig. 1a), which are polyvalent cations. In contrast, heparin did not form condensates with monovalent or divalent cations (Fig. 1a). The tetravalent spermine readily formed condensates with heparin at low concentrations, while the trivalent spermidine required a fivefold higher concentration to reach the transition threshold (Fig. 1b). Furthermore, we mapped the phase diagram of heparin–spermine condensates. The upper bounds for the mapping were chosen on the basis of known concentrations of heparin[67,68] and spermine[70] in mast cells (Fig. 1c,d and Extended Data Fig. 1a). We also investigated the impact of changing the pH of the buffer and found that this had a minimal effect on condensate assembly in the range of physiologically relevant pH of body fluids (Extended Data Fig. 1b). In addition to heparin, chondroitin sulfate is another major glycosaminoglycan synthesized in mast cells[71], which is structurally close to heparin and also highly negatively charged. We found that chondroitin sulfate formed condensates with spermine, whether alone or mixed with heparin at varying stoichiometries (Extended Data Fig. 1c), suggesting that spermine could form condensates with multiple negatively charged glycosaminoglycans.

Next, we implemented microscopy approaches to further analyze the features of the spermine–heparin condensates. Using Cy5-labeled heparin and BODIPY-labeled spermine, we observed that spermine cocondensed with heparin, attaining an enriched partitioning in the condensed fraction as heparin (Fig. 1e). These data suggest that heparin and spermine form condensates through asymmetrical complex coacervation[24,27,29]. The asymmetrical complex coacervates can be formed between smaller, albeit polyvalent cations (for example, spermine) and larger, high charge-density polyanions (for example, heparin), thus tending to generate an asymmetry of molecular motions[34,35,72,73]. We used fluorescence recovery after photobleaching (FRAP) to probe for the possibility of asymmetry of molecular motions. We found minimal recovery of the heparin fluorescence following photobleaching of the condensate, in contrast to the efficient recovery of spermine fluorescence (Fig. 1f). These data suggest very limited exchange of heparin but rapid exchange of spermine between the condensed and dilute phase in this reconstitution system, thus validating the expected asymmetry of molecule motions.

Spermine is enriched in MCEGs

Next, we sought to visualize spermine and examine whether spermine colocalizes with heparin in MCEGs that derived from mast cells. We incorporated BODIPY-labeled spermine into granules synthesized in bone-marrow-derived mast cells (BMMCs)[74]. The successful incorporation of spermine was confirmed by the colocalization of BODIPY–spermine with tryptase and TNF, two major components of mast cell granules (Extended Data Fig. 2a). These spermine-labeled cells were then activated with anti-TNP IgE and TNP–BSA (IgE/Ag) for 30 min. The released granules in the medium were captured by dark avidin-coated beads (Fig. 2a). Spermine was detected within captured granules and showed an overlap with heparin (labeled by Sulforhodamine 101-conjugated avidin[57]) (Fig. 2a). Furthermore, flow cytometric analysis revealed that the majority of MCEGs (>95%) contained both spermine and heparin (Extended Data Fig. 2b, top). Their levels remained mostly stable within individual MCEGs even after 4 days when placed at 37 °C. Moreover, the MCEG number remained similar within this timeframe (Extended Data Fig. 2c). Together, these data demonstrate that MCEGs are stable entities and that spermine and heparin are core components of MCEGs.

https://doi.org/10.1038/s41589-026-02165-6

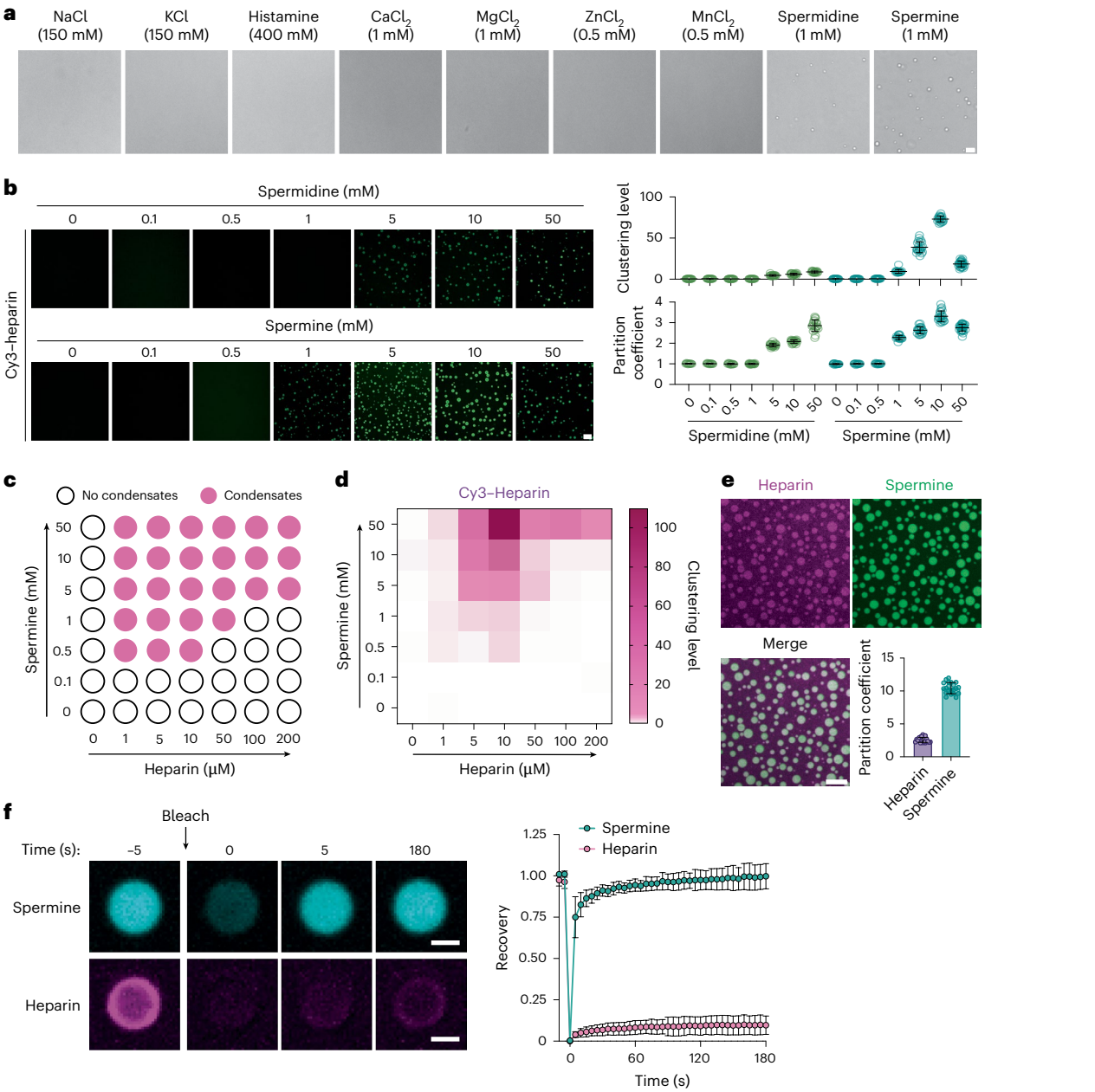

Fig. 1 | Polyamines form condensates with heparin. a, Bright-field images of 5 μM heparin in 50 mM HEPES pH 7.4 buffer in the presence of cationic salts at the indicated concentrations. Scale bar, 10 μm. **b**, Left, condensation of 50 μM FITC-labeled heparin in the presence of increasing concentrations of spermidine and spermine. The clustering level of heparin was quantified as normalized variance of heparin fluorescence and the partition coefficient of heparin was quantified as the ratio of heparin fluorescence in the dense phase to that in the dilute phase ($n = 15$ individual images per group). Scale bar, 10 μm. **c**, Low-concentration arm of the phase boundary mapped in terms of heparin (abscissa) and spermine (ordinate) concentrations. The open circles are concentrations corresponding to the one-phase regime and solid circles correspond to concentrations that place the system in the two-phase regime defined by coexisting dense and dilute phases. **d**, Quantification of clustering level of heparin condensates as shown in **c** ($n = 15$ individual images/group). **e**, Fluorescence images of heparin–spermine condensates formed by 100 μM heparin (added 2 μM Cy5–heparin; magenta) and 10 mM spermine (added 2 μM BODIPY–spermine; green). Bottom right, quantification of partition coefficients (dense-phase intensity/dilute-phase intensity) of heparin and spermine in condensates in a histogram ($n = 58$ individual condensates). Scale bar, 10 μm. **f**, FRAP of heparin–spermine condensates. Right, time course of fluorescence recovery of Cy3-labeled heparin or BODIPY–spermine in condensates formed by a total of 50 μM heparin and 5 mM spermine ($n = 17$ (heparin) or 21 (spermine) individual condensates). Scale bar, 2 μm. Data are presented as the mean ± s.d. One representative experiment from three independent experiments is shown.

To determine what protein mediators are retained in MCEGs, we performed mass spectrometry analysis on MCEGs and found that several proteases, including tryptase, chymase, CPA3 and granzyme B, were among the most abundant proteins identified (Fig. 2b and Supplementary Table 1). These proteins are within a subset of proteins identified in previous proteomic studies performed on whole mediators released by mast cells, which include both granular and soluble mediators[75]. Because of the small sizes of cytokines and chemokines, they might not be effectively detected by mass spectrometry. Therefore, we performed a multiplex cytokine profiling assay and found the presence of TNF, IL-6, granulocyte-macrophage colony-stimulating factor (GM-CSF) and CCL3 in MCEGs (Fig. 2c).

We further validated that spermine colocalized with both tryptase and TNF, the two major components within MCEGs (Fig. 2d) and that

https://doi.org/10.1038/s41589-026-02165-6

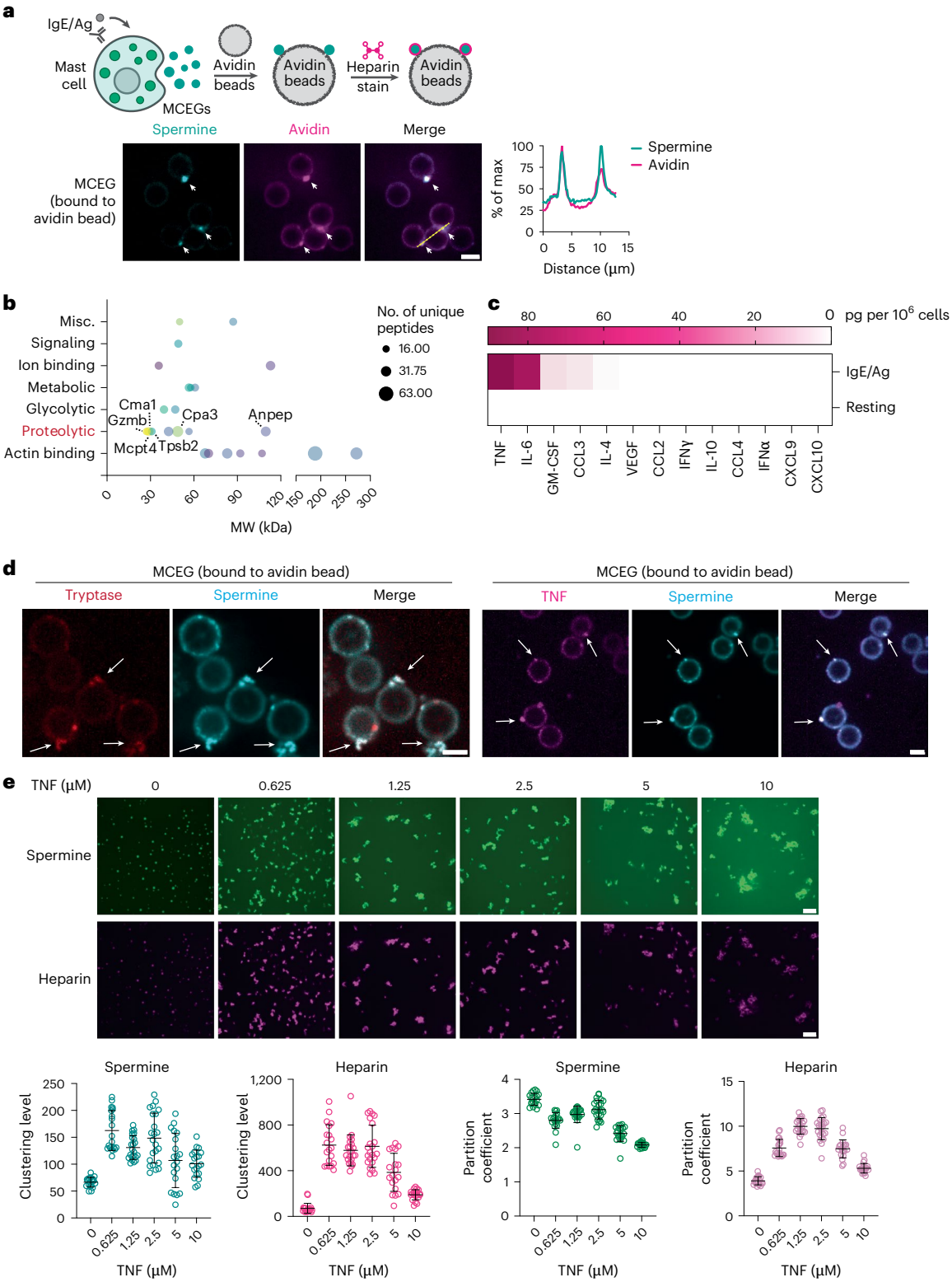

Fig. 2 | Spermine is enriched in MCEGs. a, BMMCs loaded with BODIPY–spermine (green) were stimulated with anti-TNP IgE plus TNP–BSA (IgE/Ag) for 30 min. Released granules were captured by avidin beads (top, schematic workflow) and subjected to avidin–sulforhodamine 101 (magenta) staining and fluorescence imaging (bottom left). Bottom right, quantification of fluorescence intensity of BODIPY–spermine and avidin along the indicated yellow dashed line in the merged image. Scale bar, 5 μm. **b**, Top 25 proteins identified in extracellular granules by mass spectrometry analysis were plotted against their molecular weight (MW). Gzmb, granzyme B; CMA1, chymase; Mcpt4, mast cell protease 4; Tpsb2, tryptase β2; Anpep, aminopeptidase N. **c**, TNF, IL-6, CCL3 and GM-CSF concentrations in the extracellular granules released by 1 million resting and IgE/Ag-stimulated BMMCs were measured by LEGENDplex ($n = 2$ biological replicates). IFN, interferon. **d**, MCEGs released from BMMCs expressing mCherry–tryptase (red) or mCherry–TNF (magenta) preloaded with 20 μM BODIPY–spermine (green) were collected by avidin beads and subjected to confocal imaging. White arrows denote MCEGs. Scale bar, 5 μm. **e**, Heparin–spermine condensate formation with TNF. Condensates were formed with 50 μM heparin and 5 mM spermine in the presence of indicated TNF concentrations. Bottom, quantification of the clustering levels and partition coefficients of spermine and heparin. Data represent the analysis of $n = 20$ individual images per group. Scale bar, 10 μm. Data are presented as the mean ± s.d. One representative of three independent experiments is shown.

https://doi.org/10.1038/s41589-026-02165-6

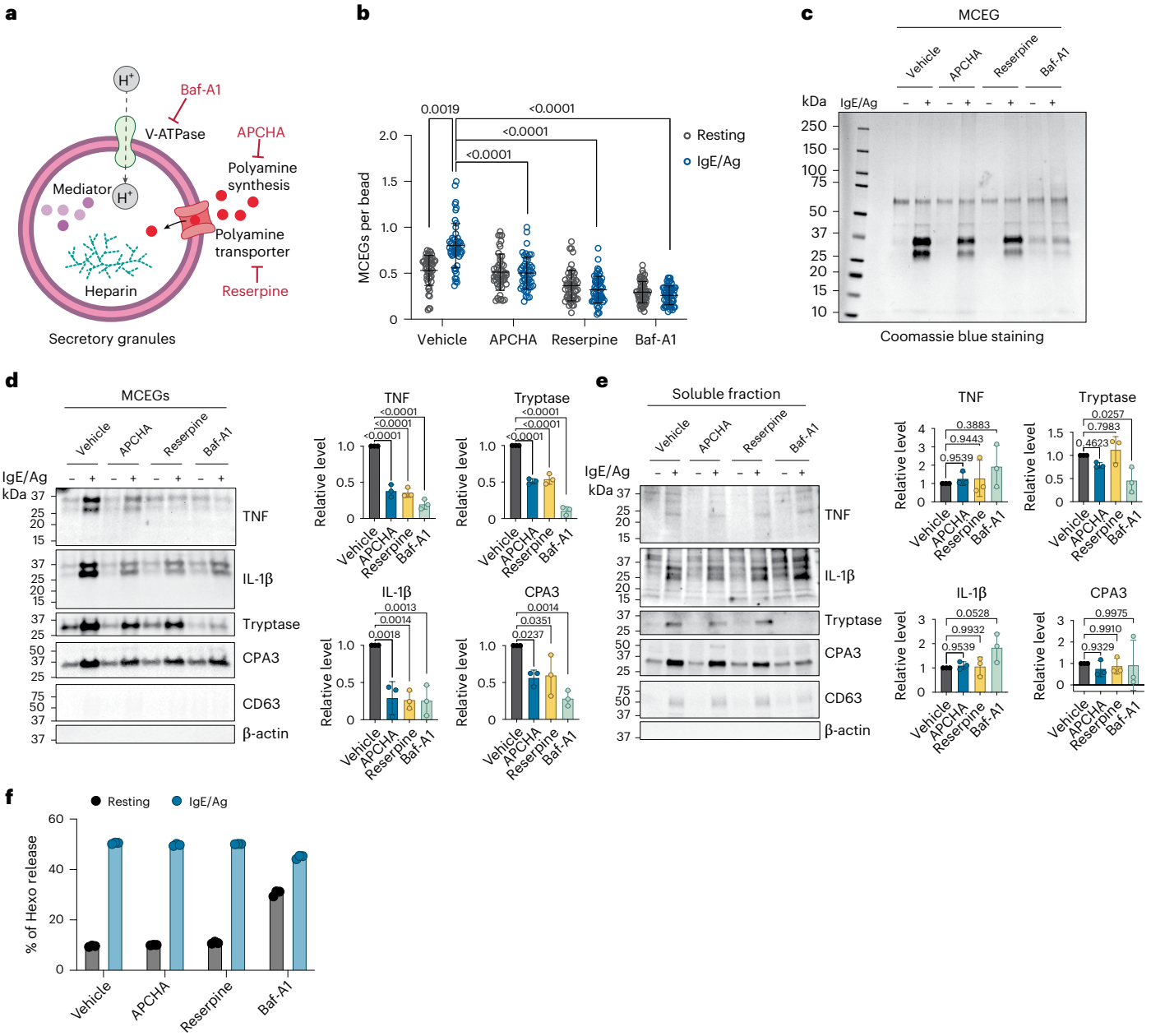

Fig. 3 | Depletion of spermine impedes MCEG assembly. a, Schematic illustration of the chemical inhibitors used in this study and their targets. **b**, MCEGs released from chemical inhibitor-treated BMMCs before and after anti-TNP IgE plus TNP–BSA (IgE/Ag) stimulation were collected with avidin beads. Granules were visualized by avidin–sulforhodamine 101 staining and the number of granules on each bead was enumerated ($n = 50$ images per group). *P* values were determined using a Kruskal–Wallis with Dunn's multiple-comparison test. **c**, Protein lysates prepared from MCEGs released by 5 million inhibitor-treated BMMCs were analyzed by SDS–PAGE and Coomassie blue staining. **d**,**e**, Western blot analysis of mast cell mediators in MCEGs (**d**) and in the soluble fraction (**e**). Band intensities for each mediator released in MCEGs (**d**) and soluble fractions (**e**) after IgE/Ag stimulation were quantified and normalized to the corresponding mediator in whole-cell lysates (Extended Data Fig. 3c). Note that TNF and IL-1β appeared as multiple bands on the blot because of different isoforms and post-translational modifications[113–116]. These bands were included in quantification. Right, all normalized values are expressed as the fold change relative to the vehicle control under IgE/Ag stimulation (set as 1) and plotted (each data point represents one independent experiment; $n = 3$). *P* values were determined using an ordinary one-way ANOVA with Dunn's multiple-comparison test. **f**, Degranulation capacity of inhibitors-treated BMMCs was analyzed by the β-hexosaminidase assay ($n = 3$ technical replicates). Data are presented as the mean ± s.d. One representative of two (**b**) or three (**c**–**f**) independent experiments is shown.

spermine and heparin were detected in nearly all TNF-containing or tryptase-containing MCEGs (Extended Data Fig. 2b, bottom). Furthermore, FRAP analysis on TNF in both MCEGs and heparin–spermine condensates revealed minimal fluorescence recovery following photobleaching, indicating that TNF was stably retained in the granules (Extended Data Fig. 2d,e).

The high stability of MCEGs likely arises from interfacial ionic crosslinks[76] formed between heparin and spermine and/or from contributions of protein components. To determine whether protein components influence the assembly of heparin–spermine condensates, we included recombinant TNF, one of the key protein components of MCEG, in the heparin–spermine condensation assay and found that TNF promoted the condensation of both heparin and spermine (Fig. 2e), suggesting that the protein components would contribute additional interactions with heparin and/or spermine that reinforce the stability of the MCEG structure. Notably, TNF distinctly modulated

the partitioning of heparin and spermine into condensates; spermine partitioning into condensates decreased progressively with increasing TNF concentrations, whereas heparin partitioning was enhanced at intermediate TNF concentrations (0.625–2.5 μM) (Fig. 2e). This differential partitioning was likely because of competitive binding between TNF and spermine for heparin, given the presence of positively charged patches on the TNF surface[77].

Depletion of spermine impedes MCEG assembly

Having observed that spermine is enriched in MCEGs, we sought to assess whether spermine is required for MCEG assembly. Spermine is synthesized in the cytosol through the polyamine biosynthesis pathway[78]; therefore, the cellular spermine level can be reduced through a chemical inhibitor *N*-(3-amino-propyl)cyclohexylamine (APCHA) against spermine synthase[79]. The reduction of spermine was validated by flow cytometry using an antibody against spermine (Extended Data Fig. 3a). Of note, we selected an intermediate concentration of APCHA to avoid cellular toxicity from the drug at high concentrations.

Next, we determined how depleting spermine affects MCEG assembly. In addition to inhibiting spermine synthesis, we included reserpine, which inhibits the polyamine transport into granules[80], and bafilomycin A1 (Baf-A1), which serves as a positive control that inhibits the vacuolar-type ATPase and disrupts the mediator storage in mast cell granules[81] (Fig. 3a). We treated BMMCs with the above drugs, followed by the release of intracellular granules to generate MCEGs using anti-TNP IgE and TNP–BSA (IgE/Ag). These are stimuli for Fc epsilon receptor I (FcεRI) that are commonly used to release mast cell granules[50,51]. MCEGs were captured by avidin beads and the number of MCEGs per bead was quantified (Extended Data Fig. 3b). Spermine inhibitors caused a profound reduction in the released granules (Fig. 3b). The total protein amount in MCEGs was also decreased (Fig. 3c). Western blot analysis revealed that the levels of TNF, IL-1β, CPA3 and tryptase in MCEGs were much lower in granules derived from APCHA-treated or reserpine-treated cells compared to the vehicle-treated cells (Fig. 3d). Importantly, the release of these mediators in soluble form (Fig. 3e) and their expression were not affected by spermine inhibitors (Extended Data Fig. 3c), suggesting that these inhibitors primarily affect mediator release in granule form rather than in soluble form. Of note, in this western blot analysis, actin (present in cytosol) and CD63 (marker for exosomes and intracellular granules) were absent in MCEGs (Fig. 3d) but present in whole-cell lysates (Extended Data Fig. 3c), indicating the purity of isolated MCEGs.

The release of β-hexosaminidase is commonly used as a marker for mast cell degranulation[48]. Of note, the released β-hexosaminidase was primarily found in the soluble supernatant of activated mast cells but not in MCEGs (Extended Data Fig. 3d), suggesting that β-hexosaminidase was predominantly exocytosed in a soluble form. This provided us with another opportunity to test whether spermine specifically affects the presence of mediators in MCEGs or whether it affects the secretion of soluble mediators as well. As a result, we found that the β-hexosaminidase levels in the supernatant of APCHA-treated and reserpine-treated BMMCs were comparable to the vehicle controls, indicating that the extent of mast cell degranulation was not affected by these inhibitors (Fig. 3f). Taken together, using inhibitors against orthogonal protein targets, we demonstrated that spermine selectively regulates the MCEG assembly without affecting the release of soluble mediators.

Condensates create a metal-ion-rich, alkaline environment

Traditionally viewed as passive mediator storage units, MCEGs house a plethora of mediators with biochemical and signaling activities[48]. To understand the functional consequences of granule assembly, we first asked whether the biochemical activities of mediators are influenced by granule assembly. We focused on CPA3, a carboxypeptidase highly enriched in MCEGs (Fig. 3d), and compared its enzymatic activity between the soluble and granule formats.

BMMCs were stimulated by anti-TNP IgE and TNP–BSA and the released granules were isolated and examined for CPA3 activity using a CPA3-specific substrate M-2245. To obtain the soluble form of CPA3 from MCEGs, the harvested granules were treated with heparinase I, which breaks down heparin[82]. Western blot analysis showed that, after heparinase I treatment, CPA3 was almost completely released into the soluble supernatant (Fig. 4a). Interestingly, CPA3 in this soluble format showed reduced enzymatic activity as compared to that in the intact granule (Fig. 4a). We verified that the presence of heparinase I did not affect the readout of this assay (Extended Data Fig. 4a). Therefore, these data suggest that CPA3 in the soluble format showed a lower protease activity than in granules.

To address the concern that the reduced protease activity of soluble CPA3 could be because of a loss of interaction or regulation by other proteins in the native granules, we performed a similar comparison using reconstituted granules in which we could accurately control the compositions. Recombinant CPA3 was mixed with heparin alone, spermine alone or heparin plus spermine, which reconstitutes the granule condensates. CPA3 was confirmed to be present in the reconstituted condensates (Extended Data Fig. 4b). We found that the protease activity of CPA3 in granules was higher than CPA3 either on its own or combined with heparin or spermine, where no condensate formation was observed (Fig. 4b).

The enhanced protease activity of CPA3 in granules could be because of a high local concentration of enzyme or a distinct chemical environment in granules. To differentiate these two possibilities, we first determined the protease activity of CPA3 with increasing concentrations (up to 50-fold). However, we found a dose-dependent decrease rather than increase in its specific activity (activity per molecule) (Extended Data Fig. 4c), disfavoring a concentration-dependent mechanism explaining the activity increase.

On the other hand, previous reports showed that the protease activity of CPA3 is regulated by pH and cations[83]. Recent studies suggested condensates that form both in vitro and in cells are characterized by interphase pH and ion gradients, thus giving rise to distinct electrochemical environments within condensates that are system specific and age dependent[31,84–87]. Motivated by these observations, we asked whether the heparin–spermine condensates create an electrochemical environment that is distinct from the surrounding dilute phase. We reconstituted the heparin–spermine condensates in a salt buffer comprising metal ions (Na^+, Ca^{2+} and Zn^{2+}) that were commonly found in the extracellular space. The dilute and dense phase were separated from the bulk solutions by centrifugation. The cation abundance was measured using inductively coupled plasma mass spectrometry[85,88]. We found that the concentrations of Na^+, Ca^{2+} and Zn^{2+}, were higher in the dense phase, showing increases of ~1.5-fold for Na^+, ~3-fold for Ca^{2+} and ~7-fold for Zn^{2+} when compared to the dilute phase (Fig. 4c). Note that the buffer contained physiologically relevant concentrations of Na^+ and Ca^{2+} (refs. 89,90) but a higher Zn^{2+} concentration than normal because the physiological relevant concentration of Zn^{2+} (nanomolar to micromolar range[91]) is below the detection limit of inductively coupled plasma mass spectrometry. Furthermore, we demonstrated that the enzymatic activities of CPA3 were enhanced with increased metal ion concentrations (Fig. 4d). Together, these data suggest that the enrichment of metal ions in the heparin–spermine condensates increases CPA3 activities.

In parallel, we determined the pH within heparin–spermine condensates using a ratiometric sensor C-SNARF-4 (refs. 31,86,92), as the electrochemical environment within condensates is strongly influenced by pH[31,86]. The interior pH was found to be 8.4, one unit higher than the external pH of 7.4 (Fig. 4e), implying a tenfold lower concentration of protons within condensates. Notably, an alkaline pH favored enhanced CPA3 activity (Fig. 4f). Using buffers mimicking both the

https://doi.org/10.1038/s41589-026-02165-6

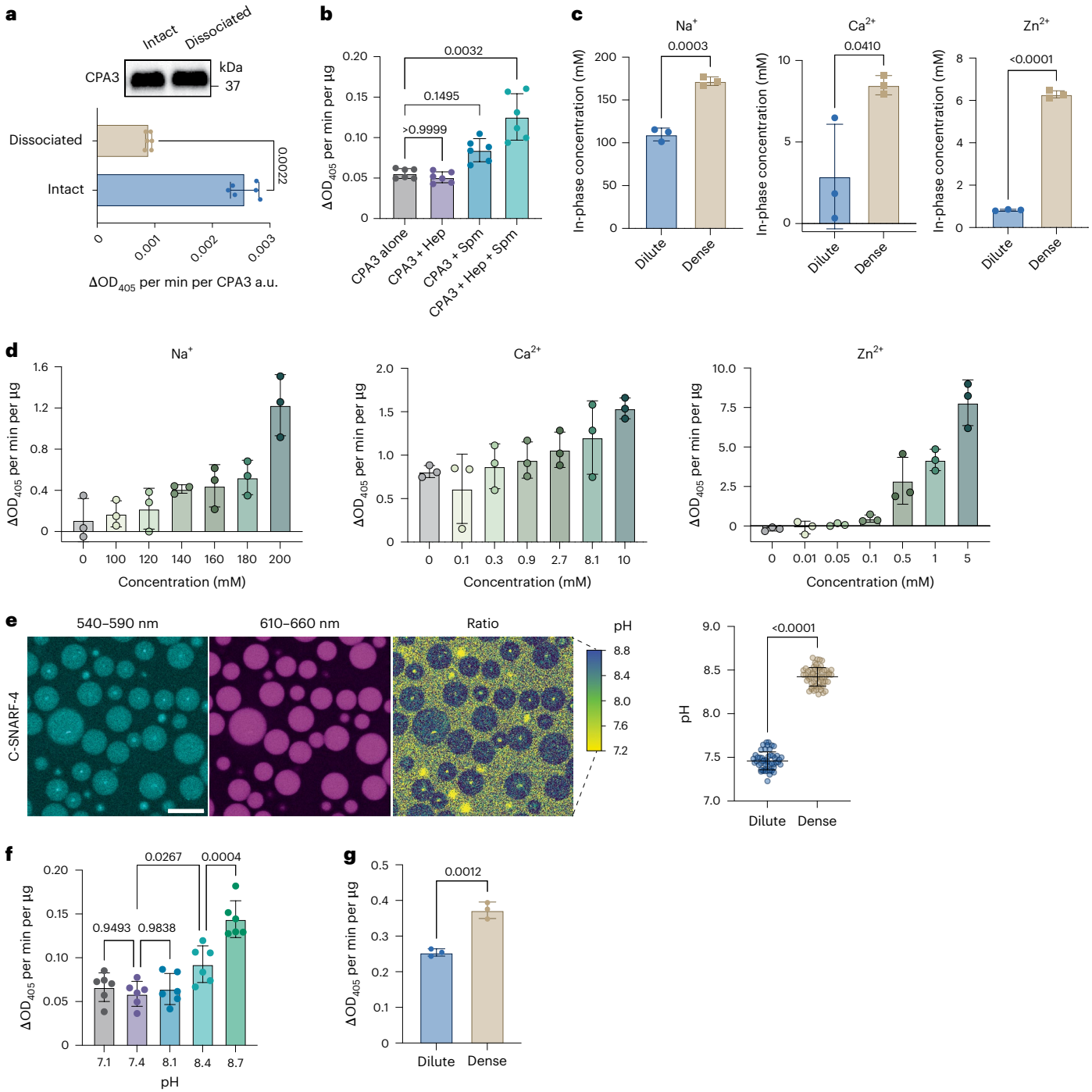

Fig. 4 | Heparin–spermine condensates create a metal-ion-rich, alkaline environment for enhanced activity of CPA3. a, CPA3 protease activities of intact native granules and of dissociated granules (treated with heparinase I) were measured using chromogenic substrate and normalized to CPA3 densitometry unit from western blot analysis ($n = 6$ biological replicates). *P* values were determined using a two-tailed Mann–Whitney test. **b**, Protease activities of recombinant CPA3 in Tyrode's buffer combined with heparin and spermine or in heparin–spermine condensates were measured ($n = 6$ biological replicates). *P* values were determined using a Kruskal–Wallis test with Dunn's multiple-comparison test. **c**, Inductively coupled plasma mass spectrometry analysis of the ion concentrations in the dilute phase and the dense phase of heparin–spermine condensates ($n = 3$ biological replicates, each with three technical replicates). *P* values were determined using a two-tailed unpaired *t*-test. **d**, Protease activities of recombinant CPA3 in 50 mM HEPES pH 7.4 buffer containing varying concentrations of NaCl, $CaCl_2$ or $ZnCl_2$ as indicated ($n = 3$ biological replicates). **e**, pH difference between the dense phase and surrounding dilute phase of heparin–spermine condensates was determined with ratiometric C-SNARF-4 dye. Right, pH values were calculated from the ratio of fluorescence intensities at 540–590 nm and 610–660 nm using a calibration curve ($n = 59$ condensates). Scale bar, 10 µm. *P* values were determined using a two-tailed unpaired *t*-test. **f**, Protease activities of recombinant CPA3 at different pH ($n = 6$ biological replicates). *P* values were determined using an ordinary one-way ANOVA with Tukey's multiple-comparison test. **g**, Protease activities of recombinant CPA3 in pH-adjusted and salt-adjusted buffers mimicking the dilute or dense conditions of heparin–spermine condensates ($n = 3$ biological replicates). *P* values were determined using a two-tailed unpaired *t*-test. Data are presented as the mean ± s.d. One representative of two (**a**,**b**,**e**) or three (**d**,**f**,**g**) independent experiments is shown.

https://doi.org/10.1038/s41589-026-02165-6

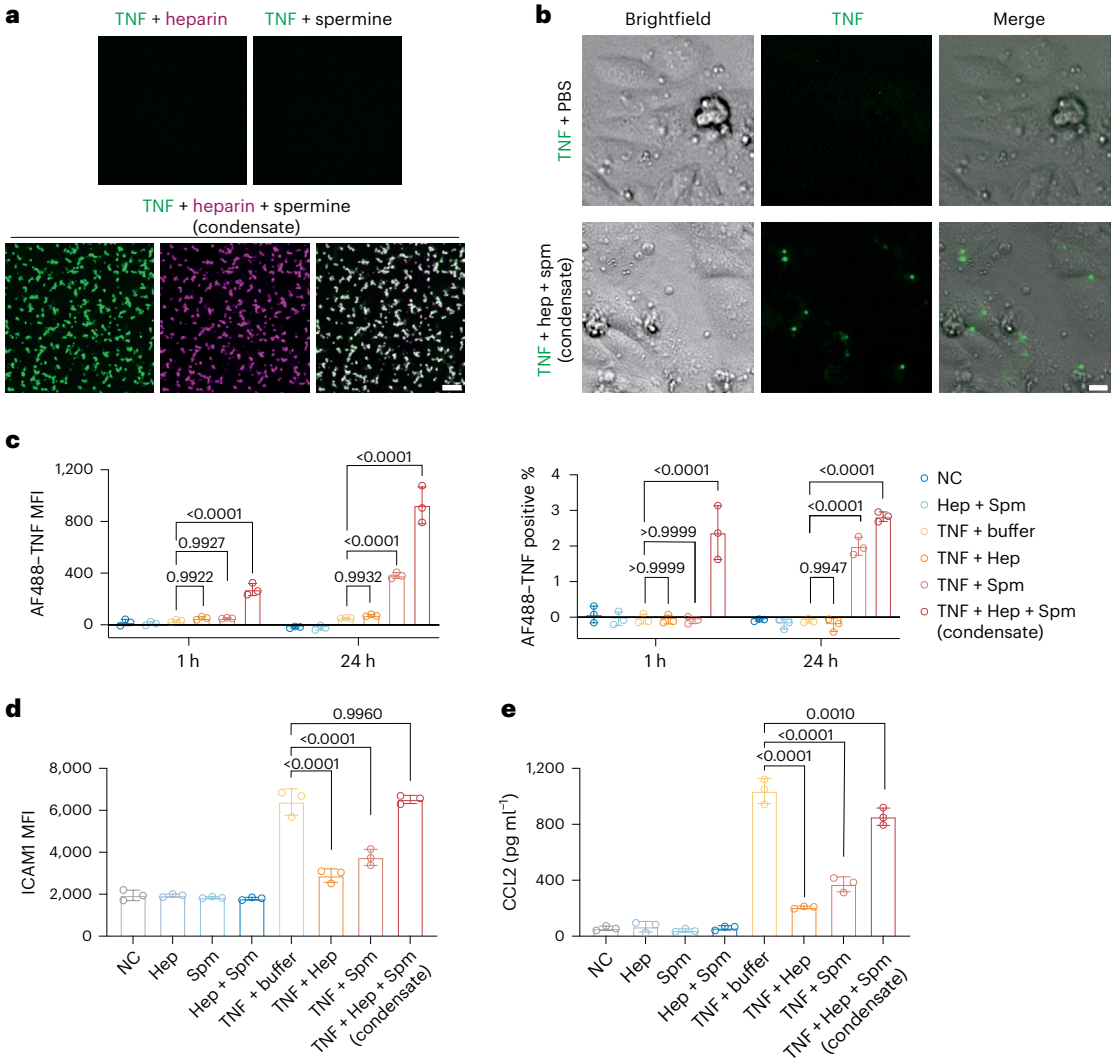

Fig. 5 | Condensation reverses the inhibition by heparin or spermine on TNF-triggered endothelial activation. a, Fluorescence images of 100 nM AF488-labeled TNF (green) in the presence of 50 μM heparin (premixed with 2 μM Cy5-labeled heparin; magenta) or 1 mM spermine or in heparin–spermine condensates. Scale bar, 10 μm. **b**, Bright-field and fluorescence images of HUVECs after 24 h of treatment with AF488-labeled TNF (1 ng, green) in PBS buffer or in heparin–spermine condensates. Hep, heparin; Spm, spermine. Scale bar, 10 μm. **c**–**e**, HUVECs were treated with 1 ng of AF488-labeled TNF in PBS buffer combined with heparin and spermine or in heparin–spermine condensates. **c**, The mean fluorescence intensity of AF488-labeled TNF on HUVECs and the percentage of AF488-labeled TNF-positive cells after 1 h and 24 h were analyzed by flow cytometry. *P* values were determined using a two-way ANOVA test with Tukey's multiple-comparison test. **d**, Surface ICAM1 expression on HUVECs was analyzed by flow cytometry. *P* values were determined using an ordinary one-way ANOVA test with Tukey's multiple-comparison test. **e**, CCL2 levels in the cell supernatant were measured by ELISA ($n = 3$ biological replicates). *P* values were determined using an ordinary one-way ANOVA test with Dunnett's multiple-comparison test. Data are presented as the mean ± s.d. One representative of three independent experiments is shown.

pH and metal ion concentrations observed in dense and dilute-phase samples, we found that CPA3 in the dense-phase buffer exhibited higher activity than in the dilute-phase buffer (Fig. 4g). Together, these results revealed a unique electrochemical environment inside heparin–spermine condensates, which regulate the biochemical activities of mediators.

Condensation reverses heparin and spermine inhibition of TNF

MCEGs enter the lymphatic and blood vessels after being released from activated mast cells in tissues[41,60]. Given that they contain mediators such as cytokines and chemokines, circulating MCEGs represent unique forms of messengers, packaged in a distinct electrochemical environment, that convey an immune signal remotely without trafficking of cells. We asked whether the granular delivery of a mediator would have a distinct functional outcome for cell-to-cell communication as compared to its soluble format. To obtain an experimental system wherein we can accurately control the condensation level and composition, we reconstituted synthetic granules in vitro with heparin, spermine and TNF, a potent immune modulator identified in mast cell granules[41,60,93,94]. The successful loading of TNF onto the heparin–spermine condensates was confirmed by confocal fluorescence microscopy (Fig. 5a). As a control, mixing TNF with either heparin or spermine (soluble TNF) did not induce condensate formation of TNF. Equal amounts of TNF in condensates or in soluble formats were added to human umbilical vein endothelial cells (HUVECs) (Fig. 5b). Substantial numbers of TNF puncta were observed on HUVECs treated with TNF in condensates but not with soluble TNF. Flow cytometric analysis revealed prolonged retention of condensed TNF on HUVECs, lasting from 1 h to 24 h. In contrast, the retention of soluble TNF was considerably lower (Fig. 5c). Interestingly, the combination of TNF and spermine also increased TNF retention on HUVECs after 24 h, albeit to a lesser extent than condensed TNF. This effect may be attributed to the subsequent interaction of

https://doi.org/10.1038/s41589-026-02165-6

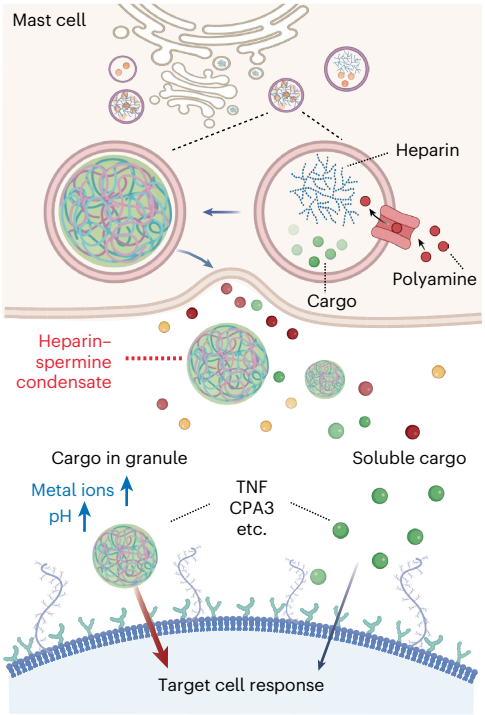

Fig. 6 | Proposed mechanism and function of MCEGs. MCEGs are assembled through electrostatic interactions between heparin and spermine. The storage of proteases and cytokines within MCEGs relies on heparin–spermine condensation. Reconstituted granules comprising heparin and spermine can efficiently capture mediators such as CPA3 and TNF, enhancing their respective enzymatic and bioactive potency. The enhanced functionality stems from the distinct electrochemical microenvironment formed within the heparin–spermine condensate, marked by elevated pH and enriched metal ions. Collectively, MCEGs represent functionally active condensates that serve as storage depots while facilitating biochemical reactions and mediating immune responses. Schematic created in BioRender; Xiong, Y. https://biorender.com/qxa3cnh (2025).

TNF and spermine with heparan sulfate on the HUVEC surface, thereby promoting its retention.

Next, we examined TNF-induced HUVEC activation. Consistent with previous reports[95], heparin alone inhibited the TNF-induced intercellular adhesion molecule 1 (ICAM1) upregulation and CCL2 production (Fig. 5d,e). Spermine alone also elicited a similar inhibition of TNF-induced activation, potentially through inhibiting the nuclear factor κB/p65 pathway that is activated by TNF[96]. In contrast, condensed TNF, which contains both heparin and spermine, induced comparable ICAM1 surface expression and CCL2 production to soluble TNF in PBS buffer. This suggests that condensed TNF is able to reverse the inhibitory effect of heparin and spermine on the functions of TNF.

Discussion

This work shows that MCEGs form through the cocondensation of polyamines with glycosaminoglycans (Fig. 6). First, heparin—used as a model glycosaminoglycan—readily forms cocondensates with polyamines in vitro. Second, depleting cellular polyamines reduces MCEG production. Third, polyamines are not only imported into the intracellular granules that generate MCEGs but also present within the extracellular MCEGs, consistent with a cocondensation mechanism. This discovery opens new avenues for applying the principles of biomolecular condensation to biological processes beyond the intracellular space, particularly for membraneless bodies that mediate cell-to-cell communication and immune responses. Furthermore, MCEGs represent a powerful model for understanding how the internal electrochemical environment of a condensate dictates the activity and function of its cargo proteins.

To definitively address MCEG function, we established a reconstitution system that recapitulates their assembly, cargo retention and chemical environment. Using this system, we demonstrated that both native MCEGs and reconstituted CPA3 granules exhibit much higher protease activity than their dissociated or soluble counterparts. We characterized the distinct electrochemical properties of these spermine–heparin condensates. Consistent with the asymmetric ion partitioning observed in protein and RNA condensates[85,87,92], the spermine–heparin condensates exhibit an alkaline pH and a high cation concentration that directly promote CPA3 activity.

MCEGs have traditionally been viewed as storage depots for fully active preformed mediators such as TNF during long-distance cell-to-cell communication[41,60]. The thinking has been that the retention of mast cell mediators, such as CPA3, tryptase and chymase from MCEG is contingent on their basic surface patches that underlie the electrostatic interactions with the negatively charged proteoglycan core[97–105]. Our work, which revealed a unique electrochemical milieu within MCEGs, suggests that MCEGs function as specialized biochemical reaction hubs. This finding demonstrates that the functional identity of MCEGs is defined by their unique internal chemical environment. Rather than being simple storage depots, they are specialized hubs where the electrochemical conditions created by complex coacervation directly regulate mediator activity. We have, thus, uncovered a form of extracellular signaling where the message is not just the molecule but the specific physicochemical context in which it is delivered. This capacity to create potent, self-contained signaling hubs outside the cell represents a fundamental advance in our understanding of the function of biomolecular condensates in cell-to-cell communication.

This notion was strengthened by our finding that granular delivery of cargo protein TNF elicits prolonged retention and sustained response on target cells, unlike soluble TNF. The functional differences between granular and soluble forms imply the contribution from structural components heparin or spermine to its cargo functions. Previous studies using cell-free systems showed that heparin association enhances the functions of its binding partners. This is achieved through various mechanisms, including direct modulation of oligomerization status for activation (for example, chemokines CCL3 and CCL5)[106], protection against proteolytic degradation (for example, tryptase)[107] or bringing substrate into close proximity for cleavage (for example, chymase)[108]. Conversely, heparin inhibits the functions of cytokines, such as IL-6 (ref. 109), interferon-γ (ref. 110), IL-10 (ref. 111) and TNF[95], by either masking their conjugations with corresponding receptors or by inducing negative effector proteins for downstream cytokine signaling. Our findings corroborated the inhibitory effect of heparin on soluble TNF[95]. Notably, the presence of spermine to form TNF–heparin–spermine condensates reversed the heparin inhibition, highlighting the functional interplay between the heparin–spermine matrix and cargo proteins within a granule. The functional importance of such a matrix environment is further supported by studies using synthetic heparin–chitosan particles, where TNF in synthetic particles exhibits sustained release kinetics[112]. These findings establish that the coacervate matrix of MCEGs dictates the ultimate signaling output of its cargo, enabling a form of context-dependent signaling. Therefore, the unique functionality conferred to mast cells by MCEGs arises from their capacity to actively tune mediator activity, transforming both the kinetics and the potency of immune messages.

Online content

Any methods, additional references, Nature Portfolio reporting summaries, source data, extended data, supplementary information, acknowledgements, peer review information; details of author contributions and competing interests; and statements of data and code availability are available at https://doi.org/10.1038/s41589-026-02165-6.

References

1. Brangwynne, C. P., Mitchison, T. J. & Hyman, A. A. Active liquid-like behavior of nucleoli determines their size and shape in *Xenopus laevis* oocytes. *Proc. Natl Acad. Sci. USA* **108**, 4334–4339 (2011).
2. Feric, M. et al. Coexisting liquid phases underlie nucleolar subcompartments. *Cell* **165**, 1686–1697 (2016).
3. Lafontaine, D. L. J., Riback, J. A., Bascetin, R. & Brangwynne, C. P. The nucleolus as a multiphase liquid condensate. *Nat. Rev. Mol. Cell Biol.* **22**, 165–182 (2021).
4. Shan, L. et al. Nucleolar URB1 ensures 3′ ETS rRNA removal to prevent exosome surveillance. *Nature* **615**, 526–534 (2023).
5. Ilik, I. A. et al. SON and SRRM2 are essential for nuclear speckle formation. *Elife* **9**, e60579 (2020).
6. Sanders, D. W. et al. Competing protein–RNA interaction networks control multiphase intracellular organization. *Cell* **181**, 306–324 (2020).
7. Yang, P. et al. G3BP1 is a tunable switch that triggers phase separation to assemble stress granules. *Cell* **181**, 325–345 (2020).
8. Guillen-Boixet, J. et al. RNA-induced conformational switching and clustering of G3BP drive stress granule assembly by condensation. *Cell* **181**, 346–361 (2020).
9. Xiao, Q., McAtee, C. K. & Su, X. Phase separation in immune signalling. *Nat. Rev. Immunol.* **22**, 188–199 (2022).
10. Banani, S. F., Lee, H. O., Hyman, A. A. & Rosen, M. K. Biomolecular condensates: organizers of cellular biochemistry. *Nat. Rev. Mol. Cell Biol.* **18**, 285–298 (2017).
11. Su, X. et al. Phase separation of signaling molecules promotes T cell receptor signal transduction. *Science* **352**, 595–599 (2016).
12. Zeng, L., Palaia, I., Saric, A. & Su, X. PLCγ1 promotes phase separation of T cell signaling components. *J. Cell Biol.* **220**, e202009154 (2021).
13. Zhang, X. et al. IDR-induced CAR condensation improves the cytotoxicity of CAR-Ts against low-antigen cancers. *Nat. Chem. Biol*. https://doi.org/10.1038/s41589-025-02031-x (2025).
14. Zeng, L. et al. Hyperactive PLCG1 induces cell-autonomous and bystander T cell activation and drug resistance. *EMBO Rep.* **26**, 4563–4586 (2025).
15. Brangwynne, C. P. et al. Germline P granules are liquid droplets that localize by controlled dissolution/condensation. *Science* **324**, 1729–1732 (2009).
16. Li, P. et al. Phase transitions in the assembly of multivalent signalling proteins. *Nature* **483**, 336–340 (2012).
17. Shin, Y. & Brangwynne, C. P. Liquid phase condensation in cell physiology and disease. *Science* **357**, eaaf4382 (2017).
18. Pappu, R. V., Cohen, S. R., Dar, F., Farag, M. & Kar, M. Phase transitions of associative biomacromolecules. *Chem. Rev.* **123**, 8945–8987 (2023).
19. Cirulis, J. T. et al. Fibrillins, fibulins, and matrix-associated glycoprotein modulate the kinetics and morphology of in vitro self-assembly of a recombinant elastin-like polypeptide. *Biochemistry* **47**, 12601–12613 (2008).
20. Yeo, G. C., Keeley, F. W. & Weiss, A. S. Coacervation of tropoelastin. *Adv. Colloid Interface Sci.* **167**, 94–103 (2011).
21. Muiznieks, L. D., Sharpe, S., Pomès, R. & Keeley, F. W. Role of liquid–liquid phase separation in assembly of elastin and other extracellular matrix proteins. *J. Mol. Biol.* **430**, 4741–4753 (2018).
22. Yu, X. et al. Heparan sulfate-dependent phase separation of CCL5 and its chemotactic activity. *Elife* **13**, RP93871 (2024).
23. Brangwynne, C. P., Tompa, P. & Pappu, R. V. Polymer physics of intracellular phase transitions. *Nat. Phys.* **11**, 899–904 (2015).
24. Veis, A. A review of the early development of the thermodynamics of the complex coacervation phase separation. *Adv. Colloid Interface Sci.* **167**, 2–11 (2011).
25. Pak, C. W. et al. Sequence determinants of intracellular phase separation by complex coacervation of a disordered protein. *Mol. Cell* **63**, 72–85 (2016).
26. Priftis, D. & Tirrell, M. Phase behaviour and complex coacervation of aqueous polypeptide solutions. *Soft Matter* **8**, 9396–9405 (2012).
27. Adhikari, S., Leaf, M. A. & Muthukumar, M. Polyelectrolyte complex coacervation by electrostatic dipolar interactions. *J. Chem. Phys.* **149**, 163308 (2018).
28. Gucht, J. V. D., Spruijt, E., Lemmers, M. & Cohen Stuart, M. A. Polyelectrolyte complexes: bulk phases and colloidal systems. *J. Colloid Interface Sci.* **361**, 407–422 (2011).
29. Wang, F., Xu, X. & Zhao, S. Complex coacervation in asymmetric solutions of polycation and polyanion. *Langmuir* **35**, 15267–15274 (2019).
30. Liu, M.-C. J. et al. Extracellular pectin–RALF phase separation mediates FERONIA global signaling function. *Cell* **187**, 312–330 (2024).
31. King, M. R. et al. Macromolecular condensation organizes nucleolar sub-phases to set up a pH gradient. *Cell* **187**, 1889–1906 (2024).
32. Farag, M., Borcherds, W. M., Bremer, A., Mittag, T. & Pappu, R. V. Phase separation of protein mixtures is driven by the interplay of homotypic and heterotypic interactions. *Nat. Commun.* **14**, 5527 (2023).
33. Galvanetto, N. et al. Extreme dynamics in a biomolecular condensate. *Nature* **619**, 876–883 (2023).
34. Boeynaems, S. et al. Spontaneous driving forces give rise to protein–RNA condensates with coexisting phases and complex material properties. *Proc. Natl Acad. Sci. USA* **116**, 7889–7898 (2019).
35. Lin, A. Z. et al. Dynamical control enables the formation of demixed biomolecular condensates. *Nat. Commun.* **14**, 7678 (2023).
36. Lu, T. & Spruijt, E. Multiphase complex coacervate droplets. *J. Am. Chem. Soc.* **142**, 2905–2914 (2020).
37. Riback, J. A. et al. Composition-dependent thermodynamics of intracellular phase separation. *Nature* **581**, 209–214 (2020).
38. Ahn, S. Y. & Obermeyer, A. C. Selectivity of complex coacervation in multiprotein mixtures. *JACS Au* **4**, 3800–3812 (2024).
39. Fisher, R. S. & Obermeyer, A. C. Viscoelasticity of globular protein-based biomolecular condensates. *Chem. Sci.* **15**, 19795–19804 (2024).
40. Smokers, I. B. A., van Haren, M. H. I., Lu, T. & Spruijt, E. Complex coacervation and compartmentalized conversion of prebiotically relevant metabolites. *ChemSystemsChem* **4**, e202200004 (2022).
41. Kunder, C. A. et al. Mast cell-derived particles deliver peripheral signals to remote lymph nodes. *J. Exp. Med.* **206**, 2455–2467 (2009).
42. Ribatti, D. Mast cells are at the interface between the external environment and the inner organism. *Front. Med. (Lausanne)* **10**, 1332047 (2023).
43. Rathore, A. P. & St John, A. L. Protective and pathogenic roles for mast cells during viral infections. *Curr. Opin. Immunol.* **66**, 74–81 (2020).
44. Galli, S. J., Gaudenzio, N. & Tsai, M. Mast cells in inflammation and disease: recent progress and ongoing concerns. *Annu. Rev. Immunol.* **38**, 49–77 (2020).
45. Plum, T. et al. Mast cells link immune sensing to antigen-avoidance behaviour. *Nature* **620**, 634–642 (2023).
46. Florsheim, E. B. et al. Immune sensing of food allergens promotes avoidance behaviour. *Nature* **620**, 643–650 (2023).
47. Liu, A. W. et al. Scratching promotes allergic inflammation and host defense via neurogenic mast cell activation. *Science* **387**, eadn9390 (2025).

48. Wernersson, S. & Pejler, G. Mast cell secretory granules: armed for battle. *Nat. Rev. Immunol.* **14**, 478–494 (2014).
49. Espinosa, E. & Valitutti, S. New roles and controls of mast cells. *Curr. Opin. Immunol.* **50**, 39–47 (2018).
50. Gaudenzio, N. et al. Different activation signals induce distinct mast cell degranulation strategies. *J. Clin. Invest.* **126**, 3981–3998 (2016).
51. Mencarelli, A. et al. Anaphylactic degranulation by mast cells requires the mobilization of inflammasome components. *Nat. Immunol.* **25**, 693–702 (2024).
52. Ghildyal, N. et al. Fate of two mast cell tryptases in V3 mastocytosis and normal BALB/c mice undergoing passive systemic anaphylaxis: prolonged retention of exocytosed mMCP-6 in connective tissues, and rapid accumulation of enzymatically active mMCP-7 in the blood. *J. Exp. Med.* **184**, 1061–1073 (1996).
53. Lindstedt, L., Lee, M. & Kovanen, P. T. Chymase bound to heparin is resistant to its natural inhibitors and capable of proteolyzing high density lipoproteins in aortic intimal fluid. *Atherosclerosis* **155**, 87–97 (2001).
54. Schwartz, L. B., Riedel, C., Caulfield, J. P., Wasserman, S. I. & Austen, K. F. Cell association of complexes of chymase, heparin proteoglycan, and protein after degranulation by rat mast cells. *J. Immunol.* **126**, 2071–2078 (1981).
55. Dvorak, A. M. Ultrastructural studies of human basophils and mast cells. *J. Histochem. Cytochem.* **53**, 1043–1070 (2005).
56. Kokkonen, J. O., Lindstedt, K. A. & Kovanen, P. T. Metabolism of LDL in mast cells recovering from degranulation. Description of a novel intracellular pathway leading to proteolytic modification of the lipoprotein. *Arterioscler. Thromb.* **13**, 276–285 (1993).
57. Joulia, R. et al. Mast cells form antibody-dependent degranulatory synapse for dedicated secretion and defence. *Nat. Commun.* **6**, 6174 (2015).
58. Kokkonen, J. O. & Kovanen, P. T. Stimulation of mast cells leads to cholesterol accumulation in macrophages in vitro by a mast cell granule-mediated uptake of low density lipoprotein. *Proc. Natl Acad. Sci. USA* **84**, 2287–2291 (1987).
59. Dudeck, J. et al. Engulfment of mast cell secretory granules on skin inflammation boosts dendritic cell migration and priming efficiency. *J. Allergy Clin. Immunol.* **143**, 1849–1864 (2019).
60. Dudeck, J. et al. Directional mast cell degranulation of tumor necrosis factor into blood vessels primes neutrophil extravasation. *Immunity* **54**, 468–483 (2021).
61. Ronnberg, E., Melo, F. R. & Pejler, G. Mast cell proteoglycans. *J. Histochem. Cytochem.* **60**, 950–962 (2012).
62. Humphries, D. E. et al. Heparin is essential for the storage of specific granule proteases in mast cells. *Nature* **400**, 769–772 (1999).
63. Forsberg, E. et al. Abnormal mast cells in mice deficient in a heparin-synthesizing enzyme. *Nature* **400**, 773–776 (1999).
64. Herrera-Heredia, S. A. et al. Heparin is required for the formation of granules in connective tissue mast cells. *Front. Immunol.* **13**, 1000405 (2022).
65. Weiss, R. J., Esko, J. D. & Tor, Y. Targeting heparin and heparan sulfate protein interactions. *Org. Biomol. Chem.* **15**, 5656–5668 (2017).
66. Xue, S. et al. Phase separation on cell surface facilitates bFGF signal transduction with heparan sulphate. *Nat. Commun.* **13**, 1112 (2022).
67. Metcalfe, D. D. et al. Isolation and characterization of heparin from human lung. *J. Clin. Invest.* **64**, 1537–1543 (1979).
68. Schwartz, L. B. & Austen, K. F. Enzymes of the mast cell granule. *J. Invest. Dermatol.* **74**, 349–353 (1980).
69. Hao, C. et al. Heparin: an essential drug for modern medicine. *Prog. Mol. Biol. Transl. Sci.* https://doi.org/10.1016/bs.pmbts.2019.02.002 (2019).
70. Garcia-Faroldi, G. et al. Polyamines are present in mast cell secretory granules and are important for granule homeostasis. *PLoS ONE* **5**, e15071 (2010).
71. Stevens, R. L., Fox, C. C., Lichtenstein, L. M. & Austen, K. F. Identification of chondroitin sulfate E proteoglycans and heparin proteoglycans in the secretory granules of human lung mast cells. *Proc. Natl Acad. Sci. USA* **85**, 2284–2287 (1988).
72. Alshareedah, I., Moosa, M. M., Pham, M., Potoyan, D. A. & Banerjee, P. R. Programmable viscoelasticity in protein–RNA condensates with disordered sticker–spacer polypeptides. *Nat. Commun.* **12**, 6620 (2021).
73. Seim, I. et al. Dilute phase oligomerization can oppose phase separation and modulate material properties of a ribonucleoprotein condensate. *Proc. Natl Acad. Sci. USA* **119**, e2120799119 (2022).
74. Vanhoutte, R., Kahler, J. P., Martin, S., van Veen, S. & Verhelst, S. H. L. Clickable polyamine derivatives as chemical probes for the polyamine transport system. *ChemBioChem* **19**, 907–911 (2018).
75. Shubin, N. J. et al. Proteome analysis of mast cell releasates reveals a role for chymase in the regulation of coagulation factor XIIIA levels via proteolytic degradation. *J. Allergy Clin. Immunol.* **139**, 323–334 (2017).
76. Agrawal, A., Douglas, J. F., Tirrell, M. & Karim, A. Manipulation of coacervate droplets with an electric field. *Proc. Natl Acad. Sci. USA* **119**, e2203483119 (2022).
77. Eck, M. J. & Sprang, S. R. The structure of tumor necrosis factor-α at 2.6 Å resolution. Implications for receptor binding. *J. Biol. Chem.* **264**, 17595–17605 (1989).
78. Schibalski, R. S., Shulha, A. S., Tsao, B. P., Palygin, O. & Ilatovskaya, D. V. The role of polyamine metabolism in cellular function and physiology. *Am. J. Physiol. Cell Physiol.* **327**, C341–C356 (2024).
79. Wagner, A. et al. Metabolic modeling of single Th17 cells reveals regulators of autoimmunity. *Cell* **184**, 4168–4185 (2021).
80. Takeuchi, T. et al. Vesicular polyamine transporter mediates vesicular storage and release of polyamine from mast cells. *J. Biol. Chem.* **292**, 3909–3918 (2017).
81. Pejler, G., Hu Frisk, J. M., Sjostrom, D., Paivandy, A. & Ohrvik, H. Acidic pH is essential for maintaining mast cell secretory granule homeostasis. *Cell Death Dis.* **8**, e2785 (2017).
82. Tsai, M., Miyamoto, M., Tam, S. Y., Wang, Z. S. & Galli, S. J. Detection of mouse mast cell-associated protease mRNA. Heparinase treatment greatly improves RT–PCR of tissues containing mast cell heparin. *Am. J. Pathol.* **146**, 335–343 (1995).
83. Atiakshin, D. et al. Carboxypeptidase A3—a key component of the protease phenotype of mast cells. *Cells* **11**, 570 (2022).
84. Dai, Y. et al. Biomolecular condensates regulate cellular electrochemical equilibria. *Cell* **187**, 5951–5966 e5918 (2024).
85. Posey, A. E. et al. Biomolecular condensates are characterized by interphase electric potentials. *J. Am. Chem. Soc.* **146**, 28268–28281 (2024).
86. Hoffmann, C. et al. Synapsin condensation is governed by sequence-encoded molecular grammars. *J. Mol. Biol.* **437**, 168987 (2025).
87. Yu, W. et al. Aging-dependent evolving electrochemical potentials of biomolecular condensates regulate their physicochemical activities. *Nat. Chem.* **17**, 756–766 (2025).
88. Nageswaran, G., Choudhary, Y. S. & Jagannathan, S. Inductively coupled plasma mass spectrometry. in *Spectroscopic Methods for Nanomaterials Characterization* (eds Thomas, S., Thomas, R., Zachariah, A. K. & Mishra, R. K.) Ch. 8 (Elsevier, 2017).
89. Hansen, A. J. Effect of anoxia on ion distribution in the brain. *Physiol. Rev.* **65**, 101–148 (1985).
90. Nicholson, C., Bruggencate, G. T., Steinberg, R. & Stockle, H. Calcium modulation in brain extracellular microenvironment demonstrated with ion-selective micropipette. *Proc. Natl Acad. Sci. USA* **74**, 1287–1290 (1977).

91. Frederickson, C. J. et al. Concentrations of extracellular free zinc $(pZn)_e$ in the central nervous system during simple anesthetization, ischemia and reperfusion. *Exp. Neurol.* **198**, 285–293 (2006).
92. Dai, Y. et al. Interface of biomolecular condensates modulates redox reactions. *Chem* **9**, 1594–1609 (2023).
93. Gordon, J. R. & Galli, S. J. Mast cells as a source of both preformed and immunologically inducible TNF-α/cachectin. *Nature* **346**, 274–276 (1990).
94. Young, J. D., Liu, C. C., Butler, G., Cohn, Z. A. & Galli, S. J. Identification, purification, and characterization of a mast cell-associated cytolytic factor related to tumor necrosis factor. *Proc. Natl Acad. Sci. USA* **84**, 9175–9179 (1987).
95. Farwell, S. L. et al. Heparin decreases in tumor necrosis factor α (TNFα)-induced endothelial stress responses require transmembrane protein 184A and induction of dual specificity phosphatase 1. *J. Biol. Chem.* **291**, 5342–5354 (2016).
96. Chen, Z. et al. Spermidine activates RIP1 deubiquitination to inhibit TNF-α-induced NF-κB/p65 signaling pathway in osteoarthritis. *Cell Death Dis.* **11**, 503 (2020).
97. Stevens, R. L. & Adachi, R. Protease–proteoglycan complexes of mouse and human mast cells and importance of their β-tryptase–heparin complexes in inflammation and innate immunity. *Immunol. Rev.* **217**, 155–167 (2007).
98. Henningsson, F. et al. Altered storage of proteases in mast cells from mice lacking heparin: a possible role for heparin in carboxypeptidase A processing. *Biol. Chem.* **383**, 793–801 (2002).
99. Abrink, M., Grujic, M. & Pejler, G. Serglycin is essential for maturation of mast cell secretory granule. *J. Biol. Chem.* **279**, 40897–40905 (2004).
100. Braga, T. et al. Serglycin proteoglycan is required for secretory granule integrity in mucosal mast cells. *Biochem. J.* **403**, 49–57 (2007).
101. Hallgren, J., Backstrom, S., Estrada, S., Thuveson, M. & Pejler, G. Histidines are critical for heparin-dependent activation of mast cell tryptase. *J. Immunol.* **173**, 1868–1875 (2004).
102. Hallgren, J., Lindahl, S. & Pejler, G. Structural requirements and mechanism for heparin-dependent activation and tetramerization of human βI- and βII-tryptase. *J. Mol. Biol.* **345**, 129–139 (2005).
103. Pejler, G., Abrink, M., Ringvall, M. & Wernersson, S. Mast cell proteases. *Adv. Immunol.* **95**, 167–255 (2007).
104. Reiling, K. K. et al. Structure of human pro-chymase: a model for the activating transition of granule-associated proteases. *Biochemistry* **42**, 2616–2624 (2003).
105. Urata, H. et al. Cellular localization and regional distribution of an angiotensin II-forming chymase in the heart. *J. Clin. Invest.* **91**, 1269–1281 (1993).
106. Liang, W. G. et al. Structural basis for oligomerization and glycosaminoglycan binding of CCL5 and CCL3. *Proc. Natl Acad. Sci. USA* **113**, 5000–5005 (2016).
107. Schwartz, L. B. & Bradford, T. R. Regulation of tryptase from human lung mast cells by heparin. Stabilization of the active tetramer. *J. Biol. Chem.* **261**, 7372–7379 (1986).
108. Pejler, G. & Sadler, J. E. Mechanism by which heparin proteoglycan modulates mast cell chymase activity. *Biochemistry* **38**, 12187–12195 (1999).
109. Mummery, R. S. & Rider, C. C. Characterization of the heparin-binding properties of IL-6. *J. Immunol.* **165**, 5671–5679 (2000).
110. Litov, L. et al. Molecular mechanism of the anti-inflammatory action of heparin. *Int. J. Mol. Sci.* **22**, 10730 (2021).
111. Salek-Ardakani, S., Arrand, J. R., Shaw, D. & Mackett, M. Heparin and heparan sulfate bind interleukin-10 and modulate its activity. *Blood* **96**, 1879–1888 (2000).
112. St John, A. L., Chan, C. Y., Staats, H. F., Leong, K. W. & Abraham, S. N. Synthetic mast-cell granules as adjuvants to promote and polarize immunity in lymph nodes. *Nat. Mater.* **11**, 250–257 (2012).
113. Hata, D. et al. Involvement of Bruton's tyrosine kinase in FcεRI-dependent mast cell degranulation and cytokine production. *J. Exp. Med.* **187**, 1235–1247 (1998).
114. Murakami, M. et al. *N*-glycosylation negatively regulates the expression of tumor necrosis factor (TNF) in mouse macrophage. *Biochem. Biophys. Res. Commun.* **737**, 150897 (2024).
115. Fan, F. et al. Mast cells boost anti-tumor potency of MAIT cells via inflammasome-dependent secretion of IL-18. *Nat. Commun.* **16**, 6074 (2025).
116. Andrei, C. et al. The secretory route of the leaderless protein interleukin 1β involves exocytosis of endolysosome-related vesicles. *Mol. Biol. Cell* **10**, 1463–1475 (1999).

Methods

Mice

All animal care and experiments were approved by the Yale University Animal Care and Use Committee and in accordance with the US National Institutes of Health (NIH) guidelines. Mice were housed at the Yale University animal facilities in specific-pathogen-free conditions, maintained on a 12-h light–dark cycle in a temperature-controlled (22 °C) and humidity-controlled room. Female C57BL/6 and BALB/c mice were obtained from Envigo and used at 6–12 weeks of age for all experiments.

Cell culture

To generate BMMCs, bone marrow cells were flushed from mouse femurs and tibias and cultured in RPMI-1640 medium containing 20% FBS (Biowest), 1× penicillin–streptomycin–glutamine, HEPES, nonessential amino acids, 2-mercaptoethanol (Gibco), 20 ng ml^{-1} recombinant murine stem cell factor and 20 ng ml^{-1} recombinant murine IL-3 (Sino Biologicals). Cells were seeded at a density of 1×10^6 cells per ml and maintained at 37 °C in a 5% CO_2 humidified incubator. After 4–6 weeks, >95% of cells were confirmed mature by CD117 and FcεR1a expression with flow cytometry. HEK293T (University of California, San Francisco, Cell Culture Facility) cells were maintained in DMEM supplemented with 10% FBS and 1× penicillin–streptomycin–glutamine in a 5% CO_2 humidified incubator at 37 °C. HUVECs (American Type Culture Collection (ATCC), PCS-100-013) were cultured in vascular cell basal medium supplemented with endothelial cell growth kit BBE (ATCC) and incubated at 37 °C with 5% CO_2. Inhibitors, namely APCHA[79] (0.5 mM; TCI chemicals), reserpine[80] (10 µM; Cayman Chemical) or Baf-A1 (ref. 81) (20 nM; Cayman Chemical), were added to mast cell culture 3 days before subsequent experiments.

Plasmid construction and lentiviral transduction

DNA fragments encoding mouse Mcpt6 or Tnfa were synthesized (Genescript) and cloned into a pHR lentiviral vector in-frame with an mCherry tag at the C terminus under an SFFV promoter. For the piggyBac transposon-based system, DNA fragments encoding proteins of interest were cloned into the PB-T-PAF vector as previously described[117]. Sequences of all plasmids were verified by Sanger sequencing. Lentivirus was generated by transfection of HEK293T cells with packaging plasmids pMD2.G and psPAX2 (Addgene, plasmids 12259 and 12260) using linear polyethyleneimine hydrochloride MAX (molecular weight: 40,000; Polysciences). After 48 h, viral supernatants were collected, centrifuged, filtered using 0.45-µm filters and concentrated using Lenti-X concentrator (Takara) following the manufacturer's instructions. Virus pellets were resuspended in PBS, aliquoted and stored at −80 °C until use. BMMCs were transduced with lentivirus by spinoculation at 1,200*g* for 90 min at 32 °C. Cells were then maintained in fresh complete medium for at least 1 week before use.

Mast cell degranulation

BODIPY-conjugated spermine (20 µM; Merck, BODIPY FL conjugate) was added to BMMC culture for 2 days. The BODIPY–spermine-loaded BMMCs were then stimulated with 1 µg ml^{-1} anti-TNP IgE (BioLegend, clone TNP7) plus 100 ng ml^{-1} TNP–BSA (Cayman Chemical) (IgE/Ag) for 30 min at 37 °C in Tyrode's buffer (10 mM HEPES, 130 mM NaCl, 5 mM KCl, 1.4 mM $CaCl_2$, 1 mM $MgCl_2$ and 5.6 mM glucose, pH 7.4). After stimulation, cell supernatants were centrifuged at 500*g* for 5 min to remove cellular debris. Released heparin-containing granules from IgE/Ag-activated BMMCs were captured using avidin polystyrene beads (6.0–8.0 µm, Spherotech), incubated in the same cell supernatant for 30 min at room temperature on a rocking platform and then subjected to 10 µg ml^{-1} avidin–sulforhodamine 101 (Sigma-Aldrich) staining before confocal imaging.

To identify proteins in the MCEGs from IgE/Ag BMMCs, MCEGs were collected by centrifugation at 20,000*g* for 60 min and lysed in NuPAGE LDS sample buffer (Thermo Scientific) supplemented with protease inhibitors. After boiling at 100 °C for 5 min, granule lysates were loaded onto a 4–20% gradient gel and run for 3 min until all the samples entered the gel and stacked into a thin band. The gel was then stained with GelCode Blue (Thermo Scientific) according to the manufacturer's instructions. Protein bands with visible blue staining were excised and subjected to mass spectrometry analysis using Q-Exactive hybrid quadrupole Orbitrap mass spectrometer at the Protein Facility of Iowa State University. Mass spectrometry raw data were analyzed using Thermo Scientific's Proteome Discoverer software (version 3.1). Mass spectrometry data were searched using Mascot and Proteome Discoverer against publicly available databases on specific organism.

β-Hexosaminidase release assay

β-Hexosaminidase activities in the cell fractions were quantified with *p*-nitrophenyl-*N*-acetyl-β-D-glucosaminide (NAG; Sigma) as substrate. Cell supernatant, cell lysate and extracellular granules dissolved in 0.5% Triton buffer were incubated with NAG substrate solution (3.4 mg ml^{-1} in buffer containing 17.6 mM Na_2HPO_4 and 11.2 mM sodium citrate, pH 4.5) at 37 °C for 1 h. Reactions were stopped by adding glycine buffer (2 M Na_2CO_3 and 1.1 M glycine, pH 10). The absorbance was read at 405 nm using a SpectraMax M5 microplate reader (Molecular Devices). Background absorbance was subtracted. A standard curve was prepared using β-*N*-acetyl-hexosaminidase (0–1.6 U per ml) in parallel with the samples. Enzyme activity was calculated from the standard curve.

Protein expression and purification

HEK293T cells stably expressing His-tagged TNF proteins were generated using piggyBac transposon-based expression system following the established protocol[117]. To induce protein expression, 1 µg ml^{-1} doxycycline was added to the cell cultures maintained in serum-free DMEM for 24 h. Cell supernatant was then collected and clarified by centrifugation and filtration through 0.45-µm filters. His-tagged TNF was then bound with Ni-NTA resin (GE Healthcare), washed with buffer containing 20 mM imidazole (50 mM HEPES pH 7.4, 150 mM NaCl, 1 mM TCEP and 10% glycerol) and eluted with 500 mM imidazole buffer containing 50 mM HEPES pH 7.4, 150 mM NaCl, 1 mM TCEP and 10% glycerol. The proteins were subjected to gel-filtration chromatography using a Superdex 200 10/300 GL column (GE Healthcare) in equilibrium buffer (50 mM HEPES pH 7.4, 150 mM NaCl, 1 mM TCEP and 10% glycerol). Monomer fractions were pooled, labeled with Alexa Fluor 488 (AF488)–maleimide (Lumiprobe) for 2 h at room temperature and run through a PD MidiTrap G-25 (GE Healthcare) to remove excess dye. Protein purity was verified by SDS–PAGE and Coomassie staining.

Flow cytometry

Cell surface staining was performed by incubation of cells with antibodies in PBS containing 2% BSA for 30 min at 4 °C. The following antibodies were used: PE Cy7–FcεR1α (Clone MAR-1, Biolegend), AF488–CD117 (Clone 2B8, Biolegend) and AF647–ICAM1 (Clone HA58, Biolegend). Isotype controls were used to establish positive gates. For intracellular spermine staining, cells were fixed with 4% paraformaldehyde and then permeabilized with 0.5% saponin for 20 min. Cells were rinsed with PBS and incubated with anti-spermine antibody (Abcam, 1:500 dilution in PBS containing 2% BSA) overnight at 4 °C, followed by incubation with AF647 anti-rabbit secondary antibody (1:1,000 dilution in PBS containing 2% BSA) for 1 h at room temperature. Cells and MCEGs were analyzed on a four-laser Cytek Aurora cytometer (Cytek Biosciences), with data acquired using Cytek Spectroflo software (version 3.3.0). For MCEG quantification, CountBright absolute counting beads (Invitrogen) were spiked into MCEG samples on day 0. MCEGs were acquired in low-speed mode with a fixed volume and then normalized to the counting bead number. Data were processed using FlowJo version 10.10.0 (BD Life Sciences).

In vitro condensation assay

Heparin–spermine condensate was formed by mixing spermine and heparin solution in 50 mM HEPES pH 7.4 buffer. To visualize the condensates under fluorescence imaging, BODIPY–spermine or Cy5-labeled, FITC-labeled or Cy3-labeled heparin was added to the dark spermine or heparin buffer before mixing, reaching a final concentration of 2 μM. Condensates were incubated for 15 min at 25 °C before subsequent experiments. To separate the dense phase and dilute phase, bulk condensate sample was subjected to centrifugation at 500*g* for 10 min at room temperature. The viscous dense-phase sample was collected with a positive displacement pipette.

SDS–PAGE and western blot analysis

To analyze proteins in the MCEGs and the soluble fraction following IgE/Ag stimulation, cell suspensions were centrifuged at 500*g* for 5 min to remove cells and debris. MCEGs were isolated from the supernatant by centrifugation at 20,000*g* for 60 min. The remaining soluble fraction was concentrated using an ultracentrifugal filter (3-kDa molecular weight cutoff; Amicon). Cell pellets, MCEGs and soluble fraction were dissolved in NuPAGE LDS sample buffer (Thermo Scientific) supplemented with protease inhibitors and boiled at 100 °C for 5 min. Proteins were separated on 4–20% Mini-PROTEAN TGX stain-free protein gels (Bio-Rad) by SDS–PAGE. For Coomassie staining, gels were stained with Gelcode blue safe protein stain (Thermo Scientific) for 1 h and destained in MilliQ water (Millipore). For western blotting, proteins were transferred onto PVDF membranes (0.22 μm; Millipore), followed by blocking with 5% BSA in PBS supplemented with 0.1% Tween-20 (PBS-T). Membranes were then incubated with primary antibodies (1:1,000 dilution) in PBS-T buffer at 4 °C overnight, followed by incubation in HRP-conjugated secondary antibodies (1:10,000 dilution) in PBS-T buffer for 1 h. Protein bands were visualized using SuperSignal ECL substrate (Thermo Scientific) under a ChemiDoc XRS+ imaging system (Bio-Rad). The primary antibodies used were anti-TNF (clone MP6-XT22, Biolegend), anti-IL-1β (clone 3A6, Cell Signaling Technology), anti-CPA3 (Proteintech), anti-tryptase (clone 3G3, Bioss), anti-CD63 (clone NVG-2, Biolegend) and anti-β-actin (clone 13E5, Cell Signaling Technology). Secondary antibodies used were HRP-conjugated goat anti-rat IgG (H + L), goat anti-rabbit IgG (H + L) and goat anti-mouse IgG (H + L) (all from Thermo Scientific).

Confocal imaging and FRAP

Confocal imaging and FRAP experiments were performed on microscope system composed of a Nikon Ti2-E inverted motorized microscope stand, motorized stage with stagetop Piezo, Lapps system with XY miniscanner for 405-nm FRAP, CSU-X1 spinning disk confocal microscope, Agilent laser combiner with four lines (405, 488, 561 and 640 nm) and scientific complementary metal–oxide–semiconductor camera Photometrics Prime 95B. Images were acquired using a Nikon ×60 Plan Apo (1.40 numerical aperture (NA)) oil-immersion objective with NIS Elements software and analyzed in Fiji (ImageJ2, 2.16.0/1.54p). Imaging of condensates was performed on mPEG-silane-passivated (Laysan Bio) coverslips[118], which were precleaned with 5% Hellmanex III (Sigma) and etched with 5 M NaOH. The fluorescence clustering level was quantified using normalized variance (σ^2/μ), calculated by dividing the square of the s.d. by the mean fluorescence intensity across the entire image. The partition coefficient, reflecting the enrichment of fluorescence in condensates, was determined by measuring the ratio of fluorescence intensity in dense phases to that in dilute phases. For confocal imaging of BMMC or MCEG-bound avidin beads, samples were imaged on a glass-bottom 384-well plate (CellVis). For FRAP, a region of interest (ROI) was photobleached using a 405-nm FRAP laser. Fluorescence recovery was monitored over 3 min at 5-s intervals. Before photobleaching, four baseline images at 5-s intervals were recorded. For each time point, the fluorescence of an unbleached region was measured as a reference to correct for nonspecific photobleaching. The fluorescent intensity of bleached ROI over time was quantified with background fluorescence subtracted, corrected by the unbleached region at the same time point and then normalized to the prebleached intensity of the ROI (set as 1).

Inductively coupled plasma mass spectrometry

A bulk condensate sample was prepared by mixing 2 ml of 1 mM heparin solution with 18 ml of 10 mM spermine solution in 50 mM HEPES pH 7.4 buffer supplemented with salts. The final salt concentrations in the mixture were 150 mM NaCl, 1 mM $CaCl_2$, 5 mM KCl, 5 mM $MgCl_2$, 500 μM $ZnCl_2$ and 500 μM $MnCl_2$. The bulk sample was centrifuged at 500*g* for 10 min to separate the dilute and dense phases. Then, 8 μl of each phase was pipetted into borosilicate glass tubes containing 0.5 ml of nitric acid (70%, trace metal grade; Fisher Chemical). Samples were boiled at 90 °C for 2 h with glass coverslips placed on the tubes to minimize evaporation and then cooled to room temperature. Samples were further diluted with 16.5 ml of 2% nitric acid (v/v in deionized water) and analyzed using a NexION 2000 inductively coupled plasma mass spectrometer (PerkinElmer) equipped with a dynamic reaction cell and autosampler (PerkinElmer), as previously described[85]. For calibration, standard solutions containing a mixture of sodium, potassium, calcium, zinc, magnesium and manganese at serial concentrations were prepared in 2% nitric acid (v/v). Standards were analyzed before and after dilute-phase and dense-phase sample measurements to ensure instrument stability throughout the experiment in addition to a scandium internal standard. Raw counts per second (cps) data for standards, dilute-phase samples and dense-phase samples were recorded. Data were processed by normalizing cps values to the calibration curves with internal standard and accounting for dilution factors.

pH measurement with C-SNARF-4

The ratiometric pH-sensitive dye C-SNARF-4 (Thermo Scientific) was used to measure pH inside and outside condensates, following an established protocol[92]. Samples containing C-SNARF-4 (20 μM) were loaded on a glass-bottom 384-well plate and imaged on a Leica SP8 equipped with an HC PL APO ×40 (1.30 NA) oil-immersion objective. Imaging was performed using a constant 75% white-light laser power with excitation at 531 nm. Emission signals were acquired in two channels, 540–590 nm and 610–660 nm. To establish a calibration curve, a series of 50 mM Tris buffers (pH range: 7–9) was prepared and mixed with C-SNARF-4 probe (20 μM). Fluorescence images of the calibration samples were acquired under identical imaging conditions. The ratio of fluorescence intensity (540–590 nm/610–660 nm) was calculated in FIJI (ImageJ) and plotted against the actual pH values measured with a calibrated pH meter (Mettler Toledo). Sample pH values were determined by applying the measured fluorescence intensity ratio to the calibration curve.

CPA3 protease activity assay

CPA3 protease activity was measured using the chromogenic substrate *N*-(4-methoxyphenylazoformyl)-Phe-OH potassium salt (M-2245; Bachem). Reactions were initiated by mixing 5 μl of sample (100 nM) with 50 μl of M-2245 substrate stock (1 mM). Absorbance at 405 nm was recorded over 10 min at 15-s intervals using a SpectraMax microplate reader (Molecular Devices). Cleavage of M-2245 results in a decrease in absorbance at 405 nm. The enzyme activity was determined from the initial linear phase of the absorbance–time curve, typically within the first 2 min of the assay. CPA3-specific activity was expressed as differences in absorbance at 405 nm per min per μg of CPA3.

Statistics

Statistical analysis was performed using GraphPad Prism version 10.4.0. Data are presented as the mean or mean ± s.d. as indicated. When comparing the means of two groups, a two-tailed unpaired Student's

t-test or Mann–Whitney *U*-test for nonparametric data was used. When comparing more than two groups, a one-way or two-way analysis of variance (ANOVA) followed by multiple-comparison test was used.

Reporting summary

Further information on research design is available in the Nature Portfolio Reporting Summary linked to this article.

Data availability

Data supporting the findings of this study are available in the main article and its Supporting Information. Source data are provided with this paper.

References

117. Li, Z., Michael, I. P., Zhou, D., Nagy, A. & Rini, J. M. Simple piggyBac transposon-based mammalian cell expression system for inducible protein production. *Proc. Natl Acad. Sci. USA* **110**, 5004–5009 (2013).
118. Gidi, Y., Bayram, S., Ablenas, C. J., Blum, A. S. & Cosa, G. Efficient one-step PEG-silane passivation of glass surfaces for single-molecule fluorescence studies. *ACS Appl. Mater. Interfaces* **10**, 39505–39511 (2018).

Acknowledgements

We thank S. Galli, R. Sagi-Eisenberg, S. Abraham and Y. Dai for feedback on the manuscript. X.S. was supported by an American Cancer Society Research Scholar Grant (135926), the National Institute of General Medical Sciences Maximizing Investigators' Research Award program (R35 GM138299), the Gabrielle's Angel Foundation Medical Research Award, the Pershing Square Sohn Prize for Young Investigators in Cancer research, the National Cancer Institute Exploratory/Developmental Research Grant (R21 CA286364), the NIH Exploratory/Developmental Bioengineering Research Grant (R21 CA294038), the Human Frontier Science Program Early-Career Research Grant (RGY0088/2021), the Yale Liver Center Pilot Award (P30 DK034989), the Yale Lion Heart Pilot Grant, the NIH Director's Transformative Research Award (EB037112) and the Department of Defense Congressionally Directed Medical Research Programs Ovarian Cancer Research Program Investigator-Initiated Research Award (OC240151, HT9425-25-1-0598). R.V.P. was supported by the US National Science Foundation (grant MCB-2227268) and the St. Jude Children's Research Hospital collaborative on the Biology and Biophysics of RNP Granules.

Author contributions

Y.X. and X.S. conceptualized the project. Y.X designed and performed the experiments and analyzed the data. J.G., K.S., L.Z., Y.T., M.S. and A.A. designed the experiments and contributed to reagent preparation. D.T.T. and A.P. performed the inductively coupled plasma mass spectrometry under the supervision of R.V.P. Y.X., X.S. and R.V.P. wrote the manuscript with input from all the other authors.

Competing interests

R.V.P. is a member of the scientific advisory board of and shareholder in Dewpoint Therapeutics. The other authors declare no competing interests.

Additional information

Extended data is available for this paper at https://doi.org/10.1038/s41589-026-02165-6.

Supplementary information The online version contains supplementary material available at https://doi.org/10.1038/s41589-026-02165-6.

Correspondence and requests for materials should be addressed to Rohit V. Pappu or Xiaolei Su.

Peer review information *Nature Chemical Biology* thanks Pu Gao, Roy Parker and Ronit Sagi-Eisenberg for their contribution to the peer review of this work.

https://doi.org/10.1038/s41589-026-02165-6

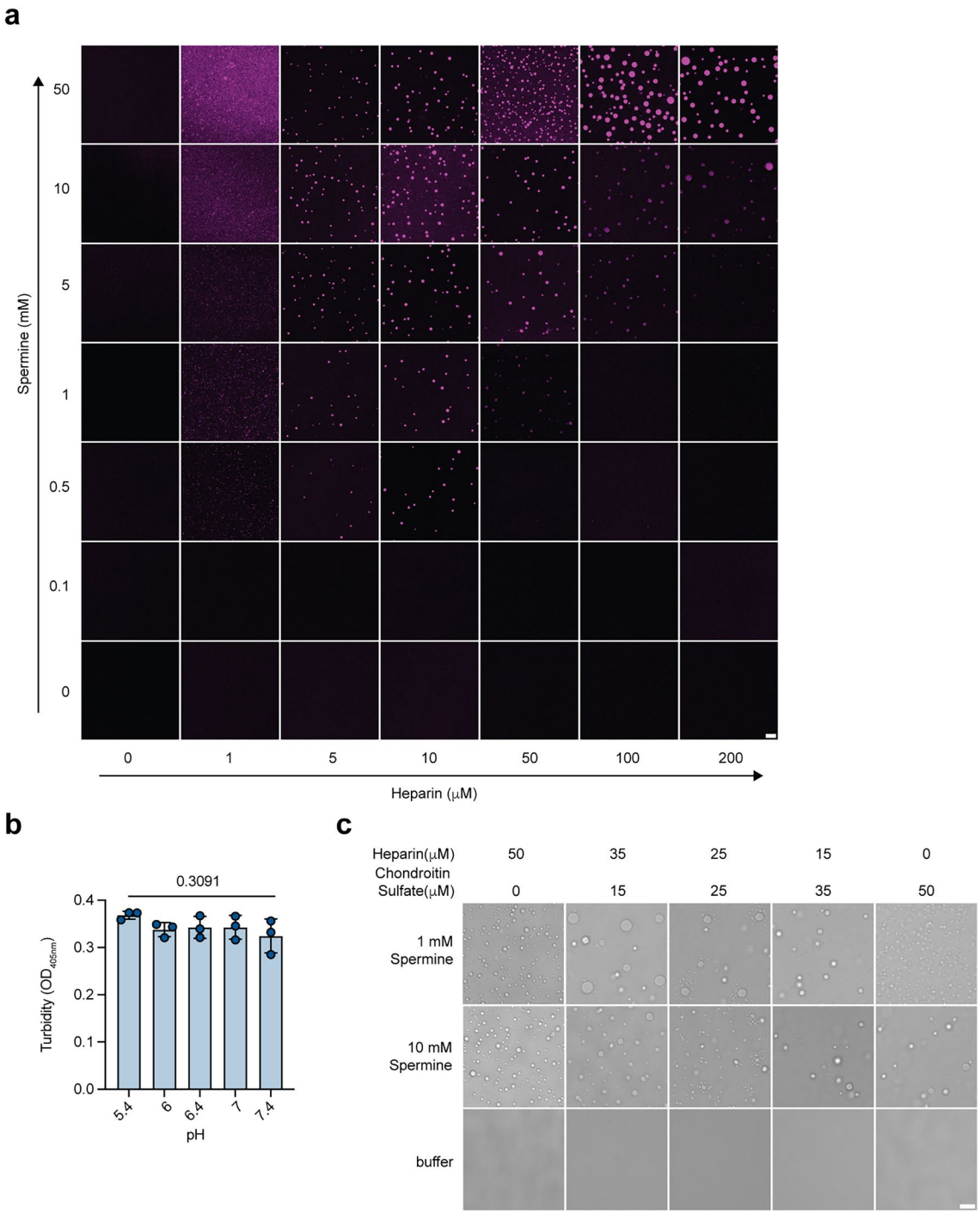

Extended Data Fig. 1 | Polyamines form condensates with heparin. **a**, Fluorescent images of Cy3-labeled heparin in the presence of increasing concentrations of spermine in 50 mM HEPES, pH 7.4 buffer related to Fig. 1c. Scale bar, 10 μm. **b**, Turbidity of heparin-spermine condensate at varying pH. Condensates were assembled by 100 μM heparin and 10 mM spermine in Na_2HPO_4-citrate buffer at the indicated pH. N = 3 biological replicates. *P* value by ordinary one-way ANOVA. **c**, Condensation of varying heparin and chondroitin sulfate concentrations in the presence of spermine. Scale bar, 10 μm. Data are presented as Mean ± SD. One representative experiment from 3 independent experiments was shown.

https://doi.org/10.1038/s41589-026-02165-6

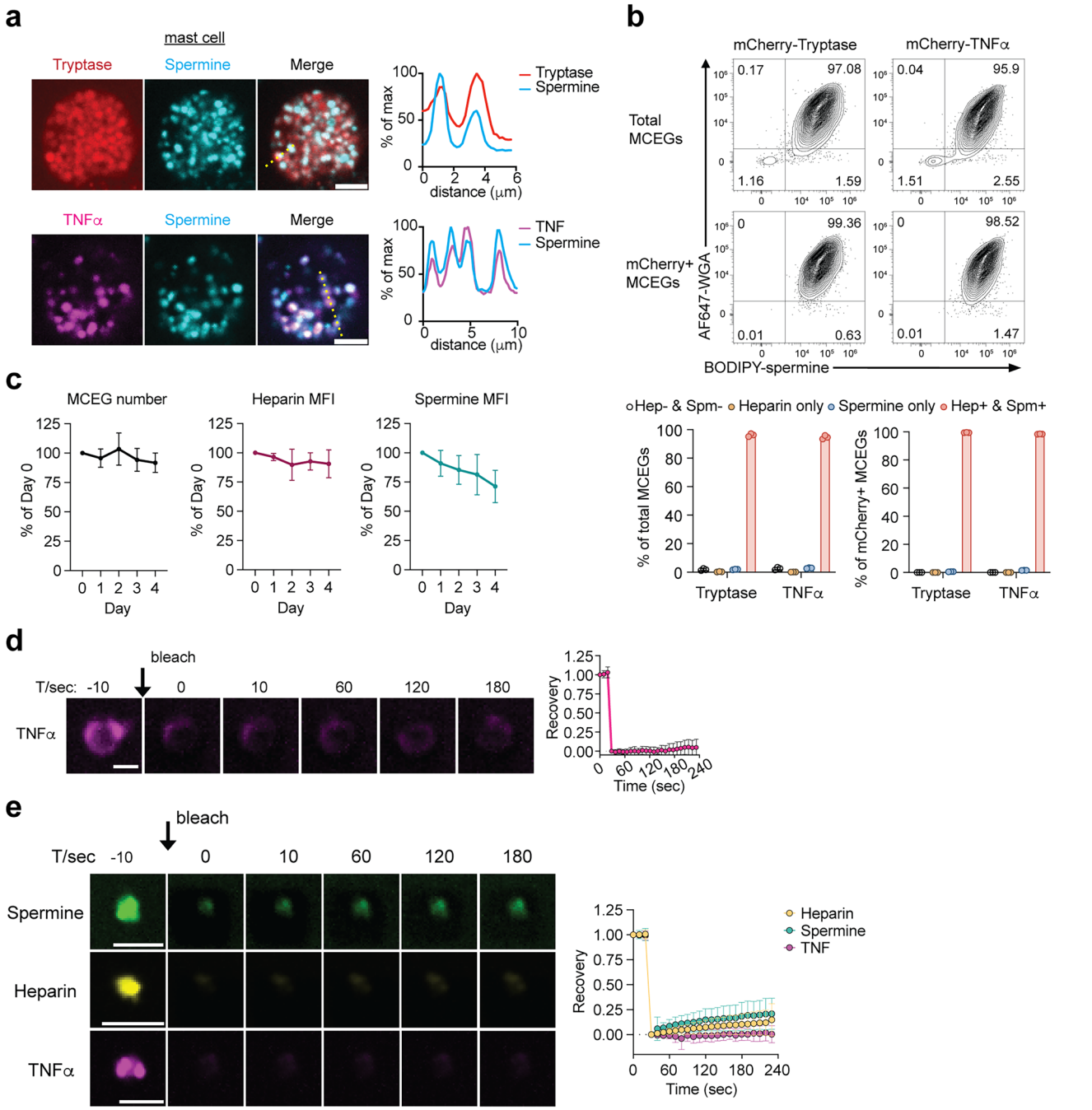

Extended Data Fig. 2 | Spermine is enriched in mast cell extracellular granules (MCEGs). a, Fluorescence images of BMMCs expressing mCherry-Tryptase (red) or mCherry-TNFα (magenta) loaded with 20 μM BODIPY-spermine (green) for 1 h. Right panels show fluorescence intensity profiles along the yellow dashed line. Scale bar, 5 μm. **b**, Flow cytometry analysis of spermine (BODIPY-spermine) and heparin (AF647-WGA) in MCEGs from BODIPY-spermine-preloaded mCherry-tryptase or mCherry-TNFα expressing BMMCs. Histograms show proportions of heparin-only, spermine-only, double positive (Hep+ & Spm+), or negative (Hep- & Spm-) MCEGs within total (left) or mCherry-mediator-retained (right) MCEG population. N = 3. **c**, MCEGs stability in heparin- and spermine-free buffers. MCEGs released from BODIPY-spermine-loaded BMMCs were incubated in tyrode's buffer at 37°C. Flow cytometry measured MCEG counts and mean fluorescent intensity (MFI) of heparin (labeled with sRd101-avidin) and BODIPY-spermine over time, normalized to Day 0 (set as 100%). N = 3. **d**, FRAP of reconstituted TNFα condensates. Right panel shows fluorescence recovery of Cy3-TNFα (1.25 μM) in reconstituted condensates (50 μM heparin, 5 mM spermine). N = 23 individual condensates. Scale bar, 2 μm. **e**. FRAP of MCEGs containing BODIPY-spermine (green), sRd101-avidin/heparin (yellow), or mCherry-TNFα (magenta). MCEGs were separated by low-speed centrifugation and photobleached in IgE/Ag stimulation supernatant. Right panel shows fluorescence recovery. N = 28 (sRd101-avidin/heparin), N = 39 (spermine), or N = 14 (TNFα). Scale bar, 5 μm. Data are presented as Mean ± SD. One representative experiment from 3 independent experiments was shown.

https://doi.org/10.1038/s41589-026-02165-6

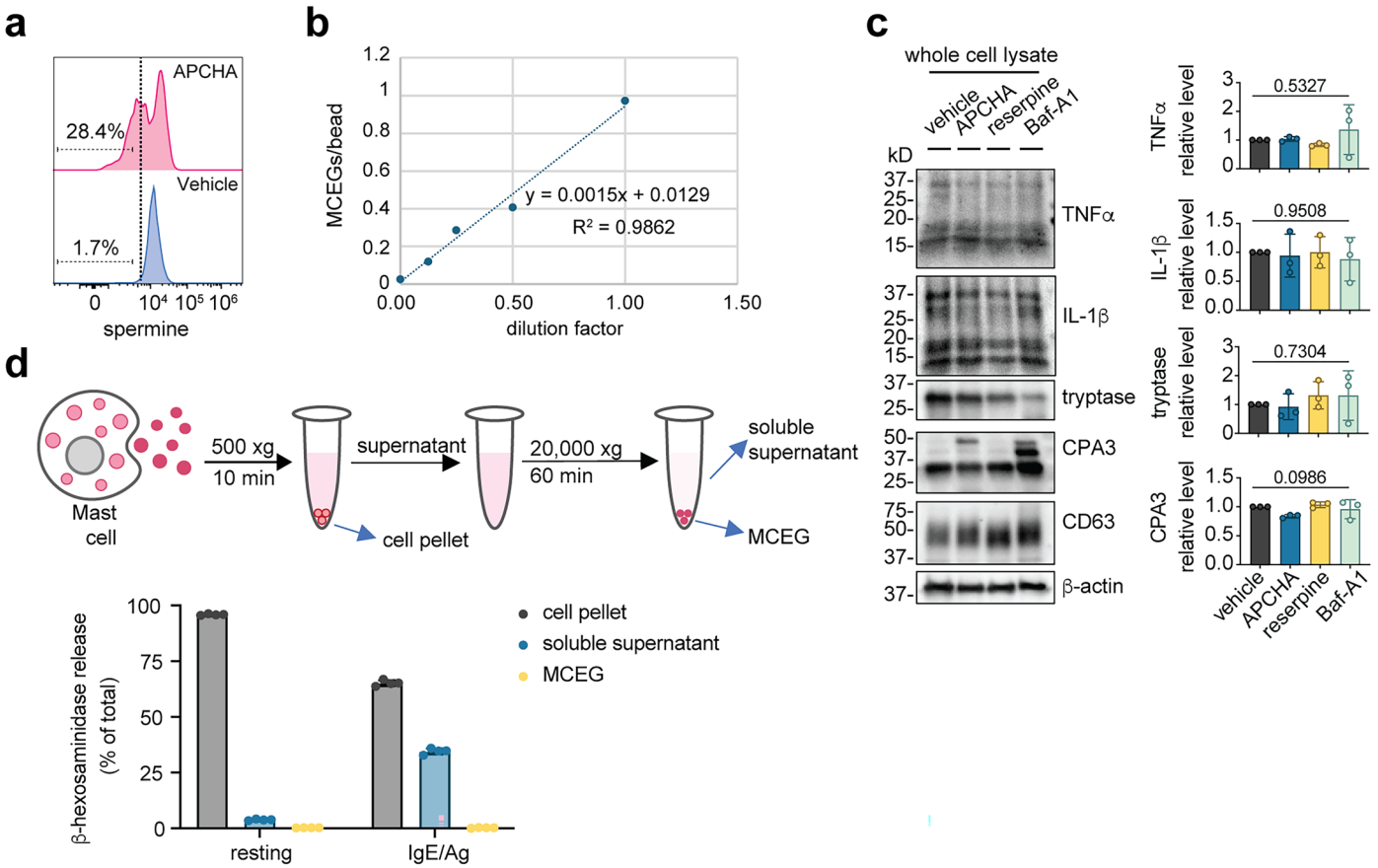

Extended Data Fig. 3 | Depletion of spermine impedes granule assembly. **a**, Spermine levels in APCHA-treated cells were determined by flow cytometry. Dashed line depicts the spermine-positive gate. **b**, Validation of avidin bead-based MCEG quantification method. Serially diluted MCEGs were incubated with equal numbers of avidin beads for 1 h at room temperature. The number of MCEGs prior to avidin bead incubation was determined by flow cytometry. The number of MCEGs per bead was plotted against the dilution factor. **c**, Western blot analysis of mast cell mediators in whole cell lysate from inhibitors-treated BMMCs. Band intensities for each mediator were quantified and normalized to β-actin. All normalized values were expressed as fold change relative to the vehicle control and plotted in the right panels (each data point represents one independent experiment, n = 3). *P* value by ordinary one-way ANOVA. **d**, Beta-hexosaminidase levels in different cell fractions as separated by centrifugation (upper panel) were expressed as percentages of total β−hexosaminidase in the cells. N = 4 biological replicates. Data are presented as Mean ± SD. One representative of three independent experiments was shown.

https://doi.org/10.1038/s41589-026-02165-6

Extended Data Fig. 4 | Heparin-spermine condensates create a metal ion-rich, alkaline environment for enhanced activity of CPA3. a, Differences in M-2245 absorbance at 405 nm per min in the presence of heparinase I, CPA3, or a combination of heparinase I and CPA3. N = 5 biological replicates. *P* value by ordinary one-way ANOVA, Tukey's multiple comparisons. **b**, Western blot analysis of CPA3 partitioning in the dilute phase and dense phase. **c**, The relative CPA3 protease activity per molecule at the indicated concentrations. N = 16 biological replicates pooled from 4 individual experiments. *P* value by Kruskal-Wallis test, Dunn's multiple comparisons. Data are presented as Mean ± SD. One representative of two (**a**, **b**) or four (**c**) independent experiments was shown.

nature portfolio

Corresponding author(s): Rohit V. Pappu and Xiaolei Su

Last updated by author(s): Jan 27, 2026

Reporting Summary

Nature Portfolio wishes to improve the reproducibility of the work that we publish. This form provides structure for consistency and transparency in reporting. For further information on Nature Portfolio policies, see our Editorial Policies and the Editorial Policy Checklist.

Statistics

For all statistical analyses, confirm that the following items are present in the figure legend, table legend, main text, or Methods section.

n/a	Confirmed
☐	☒ The exact sample size (*n*) for each experimental group/condition, given as a discrete number and unit of measurement
☐	☒ A statement on whether measurements were taken from distinct samples or whether the same sample was measured repeatedly
☐	☒ The statistical test(s) used AND whether they are one- or two-sided *Only common tests should be described solely by name; describe more complex techniques in the Methods section.*
☒	☐ A description of all covariates tested
☒	☐ A description of any assumptions or corrections, such as tests of normality and adjustment for multiple comparisons
☐	☒ A full description of the statistical parameters including central tendency (e.g. means) or other basic estimates (e.g. regression coefficient) AND variation (e.g. standard deviation) or associated estimates of uncertainty (e.g. confidence intervals)
☐	☒ For null hypothesis testing, the test statistic (e.g. *F*, *t*, *r*) with confidence intervals, effect sizes, degrees of freedom and *P* value noted *Give P values as exact values whenever suitable.*
☒	☐ For Bayesian analysis, information on the choice of priors and Markov chain Monte Carlo settings
☒	☐ For hierarchical and complex designs, identification of the appropriate level for tests and full reporting of outcomes
☒	☐ Estimates of effect sizes (e.g. Cohen's *d*, Pearson's *r*), indicating how they were calculated

Our web collection on statistics for biologists contains articles on many of the points above.

Software and code

Policy information about availability of computer code

Data collection	Protein identification with Mass Spectrometry analysis was done using Q-Exactive Hybrid Quadrupole-Orbitrap Mass Spectrometer (LC-MS/MS) at the Protein Facility of the Iowa State University. Flow cytometry data was acquired using Cytek Spectroflo software (v. 3.3.0).
Data analysis	Mass Spectrometry raw data was analyzed using Thermo Scientific's Proteome Discoverer Software (v 3.1). MS and MS/MS data was searched using Mascot and Proteome Discoverer against publicly available databases on specific organism. Flow cytometry data was analyzed using Flowjo v10.10.0. Confocal images and Western blot images were analyzed using FIJI/ImageJ2 v2.16.0/1.54p.

For manuscripts utilizing custom algorithms or software that are central to the research but not yet described in published literature, software must be made available to editors and reviewers. We strongly encourage code deposition in a community repository (e.g. GitHub). See the Nature Portfolio guidelines for submitting code & software for further information.

Data

Policy information about availability of data

All manuscripts must include a data availability statement. This statement should provide the following information, where applicable:

- Accession codes, unique identifiers, or web links for publicly available datasets
- A description of any restrictions on data availability
- For clinical datasets or third party data, please ensure that the statement adheres to our policy

Data supporting the findings of this study are available in the main article and supporting information. Source data are provided with this paper.

Research involving human participants, their data, or biological material

Policy information about studies with human participants or human data. See also policy information about sex, gender (identity/presentation), and sexual orientation and race, ethnicity and racism.

Reporting on sex and gender	not applicable
Reporting on race, ethnicity, or other socially relevant groupings	not applicable
Population characteristics	not applicable
Recruitment	not applicable
Ethics oversight	not applicable

Note that full information on the approval of the study protocol must also be provided in the manuscript.

Field-specific reporting

Please select the one below that is the best fit for your research. If you are not sure, read the appropriate sections before making your selection.

☒ Life sciences ☐ Behavioural & social sciences ☐ Ecological, evolutionary & environmental sciences

For a reference copy of the document with all sections, see nature.com/documents/nr-reporting-summary-flat.pdf

Life sciences study design

All studies must disclose on these points even when the disclosure is negative.

Sample size	Sample sizes are indicated in the respective figures with circles/dots representing each replicates and the number of repeated experiments was stated in the figure legends. Samples sizes were based on common practices in the field (eg. Nat Chem Biol, 2025, 10.1038/s41589-025-01925-0).
Data exclusions	No data was excluded for the analysis in the study.
Replication	Biological or technical replicates were shown in the figures and disclosed in the respective figure legend.
Randomization	Randomization was performed during imaging for choosing imaging fields. Randomization for sample allocation is not performed because it is not relevant to the study. All samples received identical treatment and differences emerged from intrinsic biological variation.
Blinding	Blinding is not relevant to this study since no subjective analysis was used.

Reporting for specific materials, systems and methods

We require information from authors about some types of materials, experimental systems and methods used in many studies. Here, indicate whether each material, system or method listed is relevant to your study. If you are not sure if a list item applies to your research, read the appropriate section before selecting a response.

Materials & experimental systems

n/a	Involved in the study
☐	☒ Antibodies
☐	☒ Eukaryotic cell lines
☒	☐ Palaeontology and archaeology
☐	☒ Animals and other organisms
☒	☐ Clinical data
☒	☐ Dual use research of concern
☒	☐ Plants

Methods

n/a	Involved in the study
☒	☐ ChIP-seq
☐	☒ Flow cytometry
☒	☐ MRI-based neuroimaging

Antibodies

Antibodies used	1. anti-TNP IgE (clone TNP7, BioLegend #557079) 2. PE Cy7-FceR1a (Clone MAR-1, Biolegend #134318)

3. Alexa Fluor 488-CD117 (Clone 2B8, Biolegend #105816)
4. Alexa Fluor 647-ICAM-1 (Clone HA58, Biolegend #353114)
5. anti-spermine antibody (Abcam #ab26975)
6. Alexa Fluor 647 anti-rabbit IgG (H+L) (Invitrogen #A11008)
7. anti-TNFα (clone MP6-XT22, Biolegend #506302)
8. anti-IL-1β (clone 3A6, Cell Signaling Technology #4970)
9. anti-CPA3 (Proteintech #16236-1-AP)
10. anti-CD63 (clone NVG-2, Biolegend #143902)
11. anti-tryptase (clone 3G3, Bioss #bsm-52533R)
12. anti-b-actin (clone 13E5, Cell Signaling Technology #4970)
13. HRP conjugated goat anti-rat IgG (H+L) (Thermo Scientific # 31471)
14. HRP conjugated goat anti-rabbit IgG (H+L) (Thermo Scientific #31460)
15. HRP conjugated goat anti-mouse IgG (H+L) (Thermo Scientific # 31430)

Validation

All primary antibodies used in this study were validated by the respective manufacturer for the relevant applications. Detail validation statements for all antibodies can be accessed via the manufacturer's website catalog. Where applicable, antibody specificity was further confirmed either by the use of knockout cells/samples or appropriate isotype controls, or consistency with published studies.

Eukaryotic cell lines

Policy information about cell lines and Sex and Gender in Research

Cell line source(s)	HEK 293T (University of California, San Francisco, Cell Culture Facility) Human umbilical vein endothelial cells (HUVEC; ATCC#PCS-100-013)
Authentication	The cell line vendors performed routine authentication. We will perform the STR profiling to get the most recent authentication by matching profiles of parental stocks.
Mycoplasma contamination	Verified for mycoplasma contamination, none detected.
Commonly misidentified lines (See ICLAC register)	No misidentified cell lines have been used in this study.

Animals and other research organisms

Policy information about studies involving animals; ARRIVE guidelines recommended for reporting animal research, and Sex and Gender in Research

Laboratory animals	C57BL/6 and BALB/c mice (6-12 weeks)
Wild animals	No wild animals were used.
Reporting on sex	All mice used in this study were female.
Field-collected samples	No field-collected samples were used.
Ethics oversight	All Animal care and experiments were approved by the Yale University Institutional Animal Care and Use Committee

Note that full information on the approval of the study protocol must also be provided in the manuscript.

Plants

Seed stocks	not applicable
Novel plant genotypes	not applicable
Authentication	not applicable

Flow Cytometry

Plots

Confirm that:

☒ The axis labels state the marker and fluorochrome used (e.g. CD4-FITC).

☒ The axis scales are clearly visible. Include numbers along axes only for bottom left plot of group (a 'group' is an analysis of identical markers).

☒ All plots are contour plots with outliers or pseudocolor plots.

☒ A numerical value for number of cells or percentage (with statistics) is provided.

Methodology

Sample preparation	Primary cells were isolated as described in the methods. Cell surface staining was performed by incubation of cells with antibodies in PBS containing 2% BSA for 30 min at 4°C. Following antibodies were used: PE Cy7-FceR1a (Clone MAR-1, Biolegend), Alexa Fluor 488-CD117 (Clone 2B8, Biolegend), Alexa Fluor 647-ICAM-1 (Clone HA58, Biolegend). Isotype control was used to establish positive gate. For intracellular spermine staining, cells were fixed with 4% paraformaldehyde and then permeabilized with 0.5% saponin for 20 min. Cells were rinsed with PBS and incubated with anti-spermine antibody (Abcam, 1:500 dilution in PBS containing 2% BSA) overnight at 4°C, followed by incubation with Alexa Fluor 647 anti-rabbit secondary antibody (1:1000 dilution in PBS containing 2% BSA) for 1 h at room temperature. For MCEGs quantification, CountBright Absolute Counting Beads (Invitrogen) were spiked into MCEGs samples at Day 0. MCEGs were acquired under low-speed mode with a fixed volume, , then normalized to the counting bead number.
Instrument	Cytek Aurora
Software	SpectroFlo (v. 3.3.0) for data acquisition; Flowjo v10.10.0 for data analysis
Cell population abundance	Sorting is not used in this study. For analytic analysis, the population was determined by specific antibody staining and negative control (isotype controls and negative population).
Gating strategy	The gating strategy starts from the plot of FSC-H vs. SSC-A, live cells or small particles were gated out, followed by FSC-A vs. FSC-H gating to identify the singlets. The boundary of positive and negative population was drawn based on specific antibody staining and negative controls (isotype controls and negative population).

☐ Tick this box to confirm that a figure exemplifying the gating strategy is provided in the Supplementary Information.